

See discussions, stats, and author profiles for this publication at: <https://www.researchgate.net/publication/380677872>

Unconfined turbidity current interactions with oblique slopes: deflection, reflection and combined-flow behaviours

Preprint · May 2024

DOI: 10.31223/X5569F

CITATION

1

READS

63

6 authors, including:



Ru Wang

University of Leeds

8 PUBLICATIONS 83 CITATIONS

SEE PROFILE



Edward Keavney

University of Leeds

13 PUBLICATIONS 17 CITATIONS

SEE PROFILE

TITLE

Unconfined turbidity current interactions with oblique slopes: deflection, reflection and combined-flow behaviours

AUTHORS AND AFFILIATIONS

Ru Wang^{1*}, Jeff Peakall¹, David M. Hodgson¹, Ed Keavney¹, Helena C. Brown¹ and Gareth M. Keevil¹

¹ School of Earth & Environment, University of Leeds, Leeds, LS2 9JT, UK

* Corresponding author. Ru Wang: earrwa@leeds.ac.uk

Submitted to Sedimentology for peer-review, 16th May 2024

ABSTRACT

What is the nature of flow reflection, deflection and combined-flow behaviour when gravity flows interact with slopes? In turn, how do these flow dynamics control sedimentation on slopes? Here, these questions are addressed using physical experiments, with low-density unconfined gravity flows interacting with slopes of varying gradients, at a range of flow incidence angles. The present paradigm for gravity current interaction with slopes was based on experiments with high-density flows, conducted in narrow 2D flume tanks, in small (1 m² planform) 3D tanks, or in large 3D tanks where flows can surmount the topography. Here, larger-scale physical experiments were undertaken in unconfined settings where the flow cannot surmount a planar topographic slope. The experiments show that the dominant flow-process transitions from divergence-dominated, through reflection-dominated to deflection-dominated as the flow incidence angle varies from 90° to 15° and the slope gradient changes from 20° to 40°. Also, patterns of velocity pulsing at the base of, and on, the slope vary as a function of both the flow incidence angle and slope gradient. Furthermore, in all configurations complex multidirectional combined flows are observed on, or at the base of, the slope, and are shown to vary spatially across the slope. The findings challenge the paradigm of flow deflection and reflection in existing flow-topography process models that has stood for three decades. A new process model for flow-slope interactions is presented, that provides new mechanics for the frequent observation of palaeocurrents from sole marks at high angles to those in the associated ripple division. Results provide insights into the formation and spatial distribution of distinctive combined-flow bedforms, sediment dispersal patterns, and process controls on onlap termination styles in deep-sea settings, which can be applied to refine interpretations of exhumed successions.

Keywords: unconfined turbidity current, topographic slope, incidence angle, slope gradient, flow deflection, flow reflection, combined flow, velocity pulsing

48

49 INTRODUCTION

50 Turbidity currents are subaqueous gravity-driven turbulent flows that serve as important
51 mechanisms for the transfer of large volumes of clastic sediments from the continental shelf to
52 the deep oceans (e.g., Kuenen and Migliorini, 1950; Dzulynski et al., 1959; Sestini, 1970;
53 Normark et al., 1993; Kneller and Buckee, 2000). Seafloor topography influences turbidity
54 current behaviour, and therefore the distribution and nature of their deposits. The interplay of
55 several factors need to be considered in the interaction of turbidity currents and topography
56 (Tinterri, 2011; Patacci et al., 2015; Tinterri et al., 2022 and references therein), including flow
57 duration (surge versus sustained or quasi-steady flow), the relative volume of the flow versus
58 the size of the basin ('flow confinement', hereafter; *sensu* Tőkés and Patacci, 2018; cf.
59 Pickering and Hiscott, 1985; Southern et al., 2015), and the configuration of the containing
60 topography (e.g., slope gradient, orientation and geometry; 'topographic containment',
61 hereafter). When the volume of the flow is small relative to the size of the basin, the flow can
62 expand in the basin freely, which is referred to as unconfined flow in this work. In the presence
63 of seafloor topography, flows can be reflected, deflected and/or constricted depending on the
64 configuration of the containing topography and the flow properties (e.g., thickness, viscosity,
65 and velocity).

66 A better understanding of the complicated interactions between turbidity currents and seafloor
67 topography, and the links to depositional character, is critical in a wide range of situations. For
68 example, palaeogeographic reconstruction of ancient deep-water basins (e.g., Sinclair, 1994;
69 Lomas and Joseph, 2004; Bell et al., 2018), hydrocarbon or CO₂ reservoir characterisation in
70 the subsurface (e.g., McCaffrey and Kneller, 2001; Chadwick et al., 2004; Bakke et al., 2013;
71 Lloyd et al., 2021), modern mass-flow geohazard assessment in deep-water environments (e.g.,
72 Bruschi et al., 2006; Carter et al., 2014), prediction of plastic litter and other pollutant

distribution in the deep sea (e.g., Haward et al., 2018; Kane et al., 2020) and de-risking management of sedimentation in modern human-made water reservoirs (e.g., Wei et al., 2013). The opaque nature of natural turbidity currents and limited field instrumental measurements have restricted the understanding on the interaction between turbidity currents and containing topography. Advances have been made mainly through scaled-down physical experiments (e.g., Pantin and Leeder, 1987; Muck and Underwood, 1990; Alexander and Morris, 1994; Kneller et al., 1991; Edwards et al., 1994; Amy et al., 2004; Patacci et al., 2015; Soutter et al., 2021), numerical modelling (e.g., Athmer et al., 2010; Howlett et al., 2019) and facies analysis of exhumed systems (e.g., Kneller et al., 1991; Haughton 2000; Tinterri et al., 2016, 2022). The previous experimental studies have been conducted either in narrow 2D flume tanks (e.g., Edwards et al., 1994; Amy et al., 2004; Patacci et al., 2015), in small (1 m² planform) 3D tanks (Kneller et al., 1991; Kneller, 1995), or in large 3D tanks with low-relief topographic configurations that are surmounted by the flows (Soutter et al., 2021). Field outcrop-based models of confined and contained turbidites are derived from purely theoretical analysis with limited 3D constraints (e.g., Kneller and McCaffrey, 1999; Hodgson and Haughton, 2004), or from linking to existing 2D flume experimental data (e.g., Tinterri et al., 2016, 2022). Therefore, their significance in understanding the temporal and spatial variability in the dynamics of flow-topography interactions is limited. Hence, the behaviour of 3D unconfined turbidity currents that interact with different configurations of topographic slopes has not been investigated.

Combined flows and the formation of hummock-like or sigmoidal bedforms in deep-water systems have previously been linked to the interaction of turbidity currents with topography and the superposition of a unidirectional parental turbidity current with an oscillatory component due to the reflections of the internal waves or bores against a topographic slope (Kneller et al., 1991; Edwards et al., 1994; Patacci et al., 2015; Tinterri, 2011; Tinterri et al.,

2016, 2022), largely based on the observations from 2D or qualitative 3D reflected density current experiments (e.g., Kneller et al., 1991; Edwards et al., 1994). Based on experimental observations of 3D, unconfined density currents interacting with an orthogonal planar slope, Keavney et al. (2024) propose a new mechanism for the generation of combined flows on slopes, with the absence of internal waves. However, whether the new mechanism holds in cases where 3D, unconfined density currents interact with an oblique topographic slope has not been investigated experimentally.

In this work, a series of Froude-scaled 3D physical experiments were conducted using sustained, unconfined saline density currents, where the flow was partially contained by a rigid planar slope. The flows did not overtop the barrier but were able to flow downstream around the slope. Here, dissolved salt acts as a surrogate for fine mud in suspension that does not easily settle out, and moves in bypass mode, and therefore flows used in this work can be considered to model low-density turbidity currents (Sequeiros et al., 2010). The overall aim of this work is to systematically investigate the effects of different configurations of topographic slopes on the flow behaviour, including incidence angle of the flow onto the slope and slope gradient. To achieve this, the following three objectives are undertaken: (i) to investigate the influence of containing topography on the general flow behaviour, including flow decoupling and stripping, lateral flow expansion on the slope surface, and the relative strength between flow deflection versus reflection; (ii) to explore the effect of containing topography on the temporal near-bed velocity pulsation patterns, a property that is crucial for sediment erosion and deposition; and (iii) to assess the effect of containing topography on the temporal variability of near-bed flow directions.

The results are subsequently discussed considering their implications for the development of new models of flow-topography interactions, and the generation and spatial distribution of complex, multidirectional combined flows in deep-water settings. Finally, these findings are

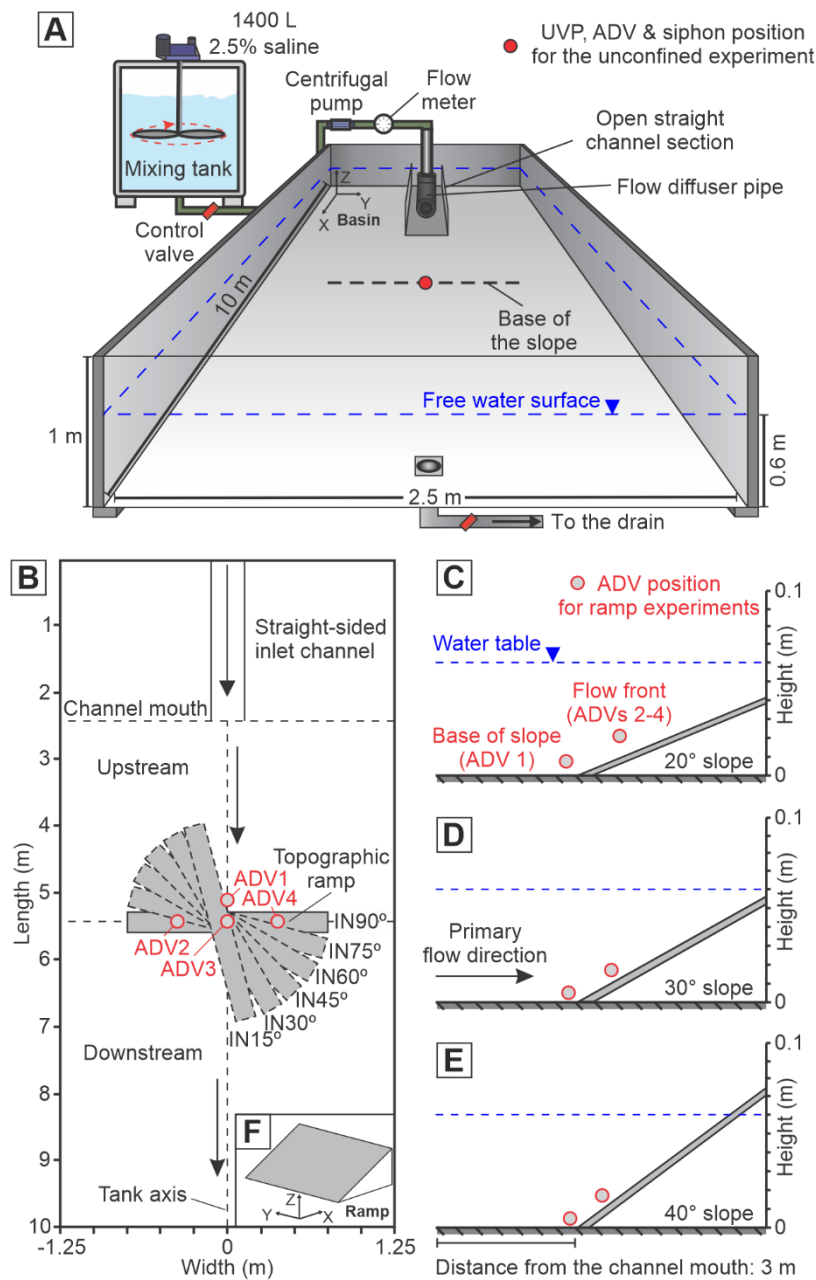
used to provide insights into the formation and spatial distribution of distinctive combined-flow bedforms, such as hummock-like and sigmoidal bedforms, sediment dispersal patterns, and process controls on onlap termination styles, which can be applied to the interpretation of exhumed successions in deep-sea settings.

METHODOLOGY

Experimental design and data collection

Experiments were conducted in the Sorby Environmental Fluid Dynamics Laboratory, University of Leeds. The flume tank used is 10 m long, 2.5 m wide and 1 m deep, with a flat basin floor (**Fig. 1A**). A 1.8 m long straight input channel section was centred in the upstream end of the main tank, through which the saline density currents entered the tank. The first experiment was run without any basin-floor topography (unconfined experiment) and served as a base-case experiment for scaling. Eighteen subsequent ramp experiments were conducted with a non-erodible, smooth, planar ramp (1.5 m wide and 1.2 m long) placed on the base of the flume tank. The ramp had a tapered leading edge at the foot abutting the basin floor, which minimized any step discontinuity. The leading edge at the foot of the ramp was placed 3 m downstream from the channel mouth (black dashed line in **Fig. 1A**), with its centrepont located on the channel-basin centreline (red circle in **Fig. 1A**). This position was chosen as the density current had lost the effects of upstream confinement and was relatively unconfined (see *Turbidity current evolution in the unconfined experiment* subsection). In these ramp experiments, the slope gradient (S) and incidence angle (IN) were systematically varied. Each experiment (**Table 1**) considers a different combination of incidence angle relative to the incoming flow (i.e., 90°, 75°, 60°, 45°, 30° and 15°; **Fig. 1B**) and ramp slope gradient (i.e., 20°, 30° and 40°; **Fig. 1C-E**). The maximum barrier height in these topographic configurations is

0.410 m, 0.585 m, and 0.76 m, respectively, and was tested to be able to fully contain the flow vertically, i.e., the density current did not surmount the topography.



149

Fig. 1. (A) Schematic sketch of the experimental facility. Note that the base of the containing topographic ramp is indicated as a black dashed line. Position of the Ultrasonic Velocity Profiler (UVP), Acoustic Doppler Velocimeter (ADV) and siphoning system for the unconfined experiment is also indicated. (B-E) Topographic configurations of the ramp experiments with different combinations of slope gradients and incidence angles relative to the incoming flow.

(B) Ramp with different incidence angles relative to the incoming flow shown in a plan view. The left-side and right-side of the tank are relative to the incoming flow. (C-E) Ramp with different slope gradients shown in a side view. Measuring localities of the four ADVs (ADV_s 1-4) for each ramp experiment are illustrated. Two sets of Cartesian coordinate systems are adopted: relative to the basin floor (A) or to the ramp (F).

Before each experiment, the main tank was filled with fresh tap water to 0.6 m deep. A saline solution of excess density 2.5% (1025 kg m^{-3}) was prepared in a 2 m^3 mixing tank with an electric rotary mixer utilised to ensure a uniform salt concentration. The saline density current was subsequently pumped into the main tank at a constant discharge rate of 3.6 L s^{-1} (**Table 1**). Water density and temperature were measured using a portable densimeter (DMA35, Anton Parr, Graz, Austria; a resolution of 0.1 kg m^{-3} and $0.1 \text{ }^{\circ}\text{C}$, respectively) in both the main tank and the mixing tank before each experimental run (**Table 1**). The discharge rate was controlled by an inverter-governed centrifugal pump and monitored in real time by an electromagnetic flowmeter (**Fig. 1A**). The density current entered the main tank through a diffuser pipe, and then flowed through the straight channel. The diffuser prevented development of a jet flow being directed straight down the tank. Each experiment started with the release of the flow from the mixing tank to the main tank and ended after a total run time of 130 s.

Unconfined experiment

In the unconfined experiment, four repeats were run using near identical initial conditions but for different purposes (**Fig. 1A**): i) flow visualisation with an overhead camera; ii) velocity profiling using an ultrasonic velocity profiler (UVP); iii) velocity profiling using an acoustic Doppler velocity profiler (ADV); and iv) density profiling using a siphon array. In the flow visualisation run, overhead images were taken by a Fujifilm X-T4 camera with Fujifilm 14 mm f/2.8R XF lens to capture the whole view of the experiment every second. Fluorescent purple

TABLE 1. Experimental parameters. T_{inflow} water temperature in mixing tank. $T_{maintank}$ water temperature in main tank. Note that four repeats were conducted for the unconfined experiment and three repeats for each ramp experiment, respectively, due to experimental constraints.

Experiment	Slope angle (°)	Incidence angle (°)	Data collected	Mean flow rate (L s ⁻¹)	T_{inflow} (°C)	$T_{maintank}$ (°C)	Inlet flow density (kg m ⁻³)
Unconfined	N/A	N/A	Flow visualisation; a UVP, ADV & density siphoning system positioned at 3 m downstream from the channel mouth along the channel-basin centreline	3.61, 3.60, 3.60, 3.60	13.2, 7.5, 12.9, 6.0	13.8, 7.9, 13.5, 6.8	1025, 1025, 1025, 1025
S20°IN90°	20	90	Flow visualisation; 4 ADVs (one positioned at the base of the slope along the channel-basin centreline and the other three at the flow front positions above the slope surface)	3.60, 3.61, 3.60	9.3, 9.6, 9.8	9.9, 10.0, 9.7	1025.1, 1025, 1024.9
S20°IN75°	20	75		3.59, 3.61, 3.60	20.9, 20.2, 20.0	21, 20.4, 20.7	1025, 1024.6, 1025
S20°IN60°	20	60		3.59, 3.60, 3.59	19.8, 19.4, 19.0	20, 19.6, 19.6	1025, 1024.6, 1024.9
S20°IN45°	20	45		3.59, 3.59, 3.59	18.5, 18.4, 18.4	19.0, 18.7, 18.7	1025.2, 1024.8, 1025
S20°IN30°	20	30		3.59, 3.60, 3.60	18.4, 18.8, 18.5	19.1, 19.0, 19.0	1025, 1025.2, 1024.8
S20°IN15°	20	15		3.60, 3.59, 3.59	18.9, 19.0, 19.2	19.4, 19.4, 19.6	1024.8, 1024.9, 1025
S30°IN90°	30	90		3.59, 3.59, 3.60	7.4, 8.0, 7.9	7.7, 7.8, 8.3	1024.9, 1024.9, 1025
S30°IN75°	30	75		3.60, 3.59, 3.59	19.2, 18.9, 19.9	19.5, 19.2, 20.1	1025.4, 1024.5, 1024.5
S30°IN60°	30	60		3.60, 3.60, 3.60	19.8, 19.8, 20.8	20.2, 21.1, 21.1	1025.2, 1024.8, 1025
S30°IN45°	30	45		3.59, 3.60, 3.59	20.1, 20.1, 20.2	20.8, 20.8, 20.6	1025, 1024.8, 1024.5
S30°IN30°	30	30		3.60, 3.60, 3.60	20.0, 19.4, 19.6	20.4, 19.8, 20.0	1024.9, 1025, 1024.6
S30°IN15°	30	15		3.59, 3.59, 3.60	20.0, 19.8, 19.8	20.4, 20.2, 20.1	1024.7, 1025, 1024.9
S40°IN90°	40	90		3.58, 3.59, 3.59	9.6, 9.7, 9.8	10.1, 10.0, 10.2	1025, 1024.9, 1025
S40°IN75°	40	75		3.60, 3.60, 3.62	19.4, 19.1, 19.3	19.8, 19.4, 19.6	1024.3, 1025.3, 1025.3
S40°IN60°	40	60		3.60, 3.60, 3.60	19.9, 19.6, 19.7	20.0, 20.0, 20.1	1024.9, 1025.3, 1025.3
S40°IN45°	40	45		3.59, 3.60, 3.59	16.9, 16.9, 16.7	17.2, 17.0, 17.0	1024.9, 1025, 1025
S40°IN30°	40	30		3.59, 3.59, 3.60	18.8, 17.8, 17.8	19.1, 18.1, 18.2	1024.9, 1025.3, 1025
S40°IN15°	40	15		3.60, 3.59, 3.60	18.7, 18.7, 17.8	19.0, 19.1, 18.2	1025.3, 1025, 1025

dye was added to the input density current to aid flow visualisation. To monitor the real-time flow properties (velocity and density) and provide a reference for the subsequent ramp experiments, velocity profiles collected by UVP and ADV systems and density profiles by a siphon system were obtained for flows at 3 m downstream from the channel mouth along the channel-basin centreline (i.e., the position of the base of the ramp in subsequent experiments; **Fig. 1A**).

UVP (Met-Flow, UVP DUO, 4 MHz; Met-Flow SA, Lausanne, Switzerland; **Fig. 2A**) was utilised to record the velocity field of the entire density current (cf. Takeda, 1991, 1993; Best et al., 2001; Lusseyran et al., 2003; Keevil et al., 2006). A vertical array of 10 UVP probes was oriented parallel to the basin floor and positioned at 0.01, 0.02, 0.03, 0.04, 0.05, 0.06, 0.07, 0.09, 0.11 and 0.13 m respectively above the basin floor (**Fig. 2A**). Each UVP probe recorded the instantaneous downstream flow velocity at 128 measurement positions along its axis extending 10 to 29 cm from the probe head in the configuration used (see **Table S1** for details of the UVP set-up).

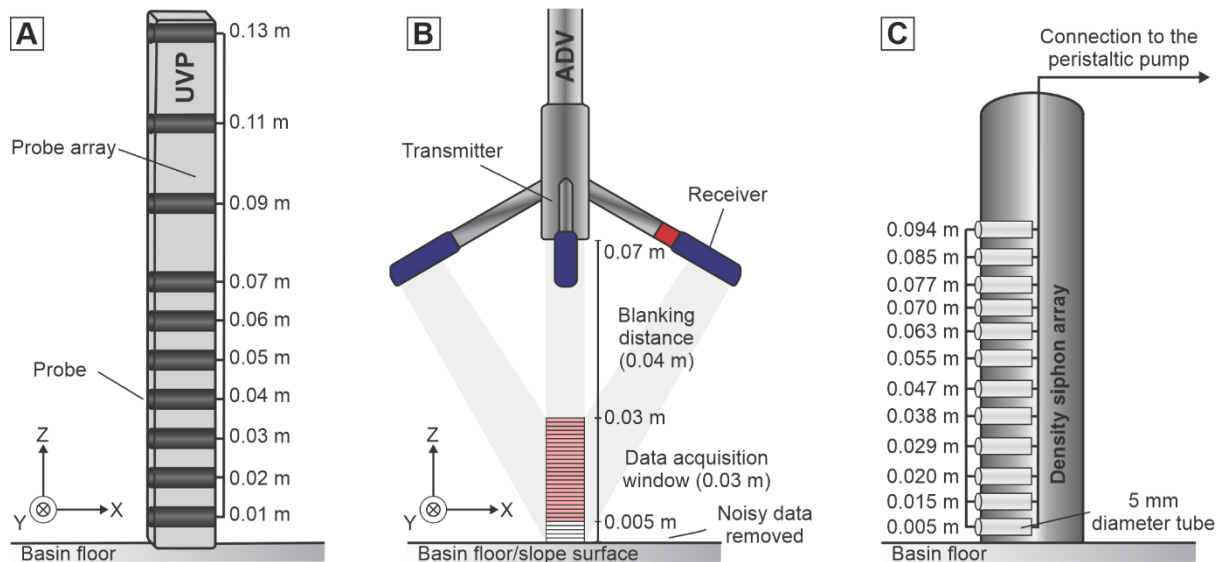


Fig. 2. Set up of (A) the UVP, (B) ADV and (C) siphoning systems in this study to measure the velocity and density profiles, respectively. All profiles were measured vertical to the basin

floor, irrespective of whether the instrument was mounted above the basin floor or the slope surface.

ADV (Nortek Vectrino Profiler; Nortek Inc., Rud, Norway; **Fig. 2B**) was used to capture the temporal evolution of the 3D velocities of the flows at a near-bed region (i.e., a coverage of 0.03 m height above the basin floor or slope surface). ADV records 3-components of velocity in bins with a vertical resolution of 1 mm (see **Table S1** for the details of the ADV set-up). The ADV data constrain the 3D velocity structure of the flows through 100 Hz measurements of instantaneous velocities (cf. 4 Hz for the UVP; **Table S1**). The measurements of the near-bed velocity are critical to understanding the conditions that effect sediment transport and deposition. Therefore, ADV was utilised in the subsequent ramp experiments to capture the near-bed velocity field of the saline density currents. During the experimental runs for the velocity profiling collection, a mixture of neutrally buoyant hollow glass spheres (Spherical 110-P8; 10 μm diameter) were seeded into the inlet flow at a constant discharge rate via a peristaltic pump throughout the experimental run (cf. Thomas et al., 2017; Ho et al., 2019). This was undertaken to enhance the reflection of the ultrasound or acoustic signal. Additionally, prior to each run, the ambient water in front of the UVP or ADV probes was also seeded with the same glass spheres to increase the signal-to-noise ratio to ca. 30 dB.

The fluid flow samples were collected by a siphoning system (**Fig. 2C**). The siphons were positioned along a vertical line and located at 0.005, 0.015, 0.020, 0.029, 0.038, 0.047, 0.055, 0.063, 0.070, 0.077, 0.085 and 0.094 m respectively above the basin floor. During the experimental run, the fluid flow was extracted from the tank via a peristaltic pump at a constant flow rate (3.9 mL s^{-1} per siphon tube). This specific value was chosen to balance obtaining enough fluid samples whilst minimising perturbations to the in-situ flow structure. After each

run, the density of the collected fluid samples was measured by the aforementioned portable densimeter.

Ramp experiments

In each ramp experimental configuration, three repeats were run using identical initial conditions but with different purposes, i.e., flow visualisation and velocity profiling by ADV systems.

In the flow visualisation runs, each experiment was recorded using up to four high-resolution video cameras (GoPro, HERO 10; GoPro, Inc., USA). One was mounted at ca. 2 m downstream from the channel mouth along the channel-basin centreline to capture the front view of the density current encountering the containing topography (i.e., ramp), two along the side of the ramp to capture the side view, and one directly on the top of the ramp surface to capture the top view. No dye was added to the inlet flow as it would provide little information on the internal fluid motion within the current. Instead, Pliolite, a low density and highly reflective polymer, and a small amount of white paint were added to the input current to help visualisation (cf. Edwards et al., 1994). The Pliolite has a subspherical shape, with a mean grain size of 1.5 mm and density of 1050 kg m^{-3} . To improve the visualisation of the density current interacting with the topographic ramp, fluorescent yellow dye was injected via a series of tubes mounted from the rear of the ramp and flush with its surface. These tubes were located at three different elevations and distributed evenly on the ramp surface (i.e., 0.15 m, 0.30 m, and 0.45 m away from the base of the ramp, respectively).

In each ramp experimental configuration, four ADVs were utilised to record the 3D flow velocity field at the near-bed region (**Fig. 1B-E** and **Fig. 2B**). One was positioned above the basin floor, at 0.02 m upstream from the base of the ramp along the channel-basin centreline

(ADV1) to capture the basal flow reversals. The other three (ADV 2-4) were placed above the slope surface to capture the temporal evolution of the velocity field near the flow front position (see *General flow behaviour* subsection). The exact locations of these three ADVs were carefully chosen based on the position of the flow front observed from the flow visualisation videos, which varied across different experiments. The transducers of the ADVs 1-4 were mounted vertically 0.07 m above the slope surface and recorded the velocity profile in thirty-one 1-mm-high cells ranging from 0 to 0.03 m above the slope surface (**Fig. 2B**). Due to experimental constraints, two sets of ADV data (ADV 1-2 and ADV 3-4) were collected in separate runs with the same initial conditions, varying the measurement locations of the ADVs in each case. The 4 ADVs were subsequently integrated to visualize the velocity field of the whole flow. During each measurement, synchronization of the two ADVs was achieved using Nortek's MIDAS data acquisition software (Nortek 2015) and the recording started from the release of the inlet flow until the flow ceased.

Experimental data analysis

All the raw instantaneous velocity data collected by the UVP and ADV systems were initially filtered in Matlab before further analysis (cf. Buckee et al., 2001; Keevil et al., 2006). First, data spikes in the time series that were more than two standard deviations from the mean were removed; here, the mean was estimated as an 11-point moving average. Second, the removed spike points were replaced by a 3-point moving mean. The ADV data closest to the boundary were affected by excess noise because of reflections. Consequently, the plotted data were clipped so that the bottom 5 data points (< 0.5 cm) were removed (**Fig. 2B**). This excess noise sometimes affected points as high as 0.7 cm above the bed, and thus for data analysis only the section between 0.7-3.0 cm above the basin floor or slope surface were utilised.

In this work, two sets of Cartesian coordinate systems were adopted, either relative to the basin floor or to the ramp (**Fig. 1A** and **1F**). The filtered 3D velocity data after the first step were corrected based on either of these two coordinate systems. When the former coordinate system is adopted, the 3D velocity components (u , v , w) are termed as streamwise, cross-stream and vertical velocities, respectively. Otherwise, they are termed as down-dip, along-strike, and vertical velocities, respectively.

The filtered instantaneous velocity data collected by the ADV system are presented as velocity time-series profiles. In these plots, positive values of the down-dip velocity depict flows travelling towards the ramp (outbound flow), whereas negative ones depict flows travelling away from the ramp and back towards the inlet (return flow). The maximum velocity (U_{max}) up/down the ramp, is taken as the highest value over the measured height range (0.7-3.0 cm) of the ADV profiles. The fluctuations in U_{max} are shown on the time series panels and serve as a representative flow down-dip velocity magnitude.

Flow scaling and characterisation

As only saline density currents are utilised in this work, Froude scaling (Yalin, 1971; Peakall et al., 1996) is used to ensure that both the dimensionless Froude and Reynolds numbers of the laboratory turbidity currents reside within appropriate flow regimes compared to natural systems (in the Froude scaling approach, the Froude number in the experimental flows should be similar to that of natural systems, while the Reynolds number is relaxed). When these scaling conditions are met, the laboratory turbidity currents can be considered scalable to natural systems.

The Reynolds number, Re , is used to characterize whether the flow is laminar or turbulent and is expressed by the ratio between the inertial forces to the viscous forces. It is given by

$$Re = \frac{\rho_s U h}{\mu} \quad (1)$$

where ρ_s represents the depth-averaged density of the current, U is the depth-averaged velocity over the flow height, h is the flow height, and μ is dynamic viscosity. Typically, flows with $Re > 2000$ are considered fully turbulent, flows with $Re < 500$ are laminar, and flows with $Re = 500-2000$ are transitional.

The Froude number, Fr_1 describes the ratio between inertial- and gravitational-forces, and is expressed as

$$Fr = \frac{U}{\sqrt{gh}} \quad (2)$$

where g denotes gravitational acceleration. Typically, flows with $Fr > 1$ are considered supercritical whereas flows with $Fr < 1$ are subcritical, though this critical value might be different in strongly stratified density currents (e.g., Sumner et al., 2013; Cartigny et al., 2014). For experiments involving density difference, such as turbidity currents, the densimetric Froude number is more physically relevant, defined by

$$Fr_d = \frac{U}{\sqrt{g'h}} \quad (3)$$

$$g' = \frac{g(\rho_s - \rho_a)}{\rho_a} \quad (4)$$

where g' represents the reduced gravitational acceleration and ρ_a denotes the density of the ambient fluid.

Based on the unconfined control experiment, the experimental density currents recorded at 3 m downstream from the channel mouth along the channel-basin centreline (i.e., the position where the centrepoint of the base of the slope resides; **Fig. 1A**) were demonstrated to have a Reynolds number of 3203 and densimetric Froude number of 0.505 (**Table 2**), and therefore

were fully turbulent and subcritical. Estimation of these two parameters is detailed in **Supporting Information 1**.

TABLE 2. Summary of the flow characteristics for the experimental density current recorded at 3 m downstream from the channel mouth along the channel-basin centreline in the unconfined reference experiment. Calculations of the mean depth-averaged downstream velocity and current density are detailed in **Supporting Information 1**.

Parameter	Value	Unit
Density of the ambient fluid (ρ_a)	999.58	kg m ⁻³
Dynamic viscosity (μ)	0.001	Pa s
Gravitational acceleration (g)	9.81	m s ⁻²
Reduced gravitational acceleration (g')	0.030	m s ⁻²
Flow depth (h)	0.11	m
Mean depth-averaged density of the current (ρ_s)	1002.6	kg m ⁻³
Mean depth-averaged downstream velocity (U)	0.029	m s ⁻¹
Maximum downstream velocity (u_p)	0.059	m s ⁻¹
Height of the maximum downstream velocity above the basin floor (h_p)	0.02	m
Reynolds number (Re)	3203	none
Densimetric Froude number (Fr_d)	0.505	none

RESULTS

Turbidity current evolution in the unconfined experiment

In the unconfined experiment, the saline density current enters the confined channel section as a highly turbulent flow with a well-developed head region, which is followed by a stable, quasi-steady body region during the rest of the experimental run (**Fig. 3A**). On exiting the confined channel section, the flow starts to spread radially and symmetrically above the flat basin floor (**Fig. 3B**). Multiple lobes and clefts can be observed at the propagating head of the density currents. A radial hydraulic jump can be observed immediately downstream of the channel-mouth location (**Fig. 3D**), suggesting that the flow regime has transitioned from a supercritical

state in the channel section to a subcritical state in the horizontal basin floor (see also **Flow scaling and characterisation** subsection). Finally, the termination of the inlet leads to a rapid decrease in current velocity and causes the current body to diminish quickly.

The representative time-averaged UVP downstream velocity profile obtained from the body region of the flows (averaging over 30 s; **Fig. 3G**) was recorded at 3 m downstream from the channel mouth along the channel-basin centreline. The velocity profile reveals a mean depth-averaged downstream velocity of 0.029 m s^{-1} , a mean depth-averaged current density of 1002.6 kg m^{-3} (i.e., 0.3% excess density) and a flow height or thickness of ca. 0.11 m (**Table 2; Supporting Information 1**). The downstream velocity reaches its maximum value ($u_p = 0.059 \text{ m s}^{-1}$) at a height of 0.02 m above the basin floor ($h_p = 0.02 \text{ m}$).

The time-averaged flow density profile at the same position (**Fig. 3G**) exhibits a noticeable exponential decrease in excess density upward, with a highest flow density ($\rho_{si} = 1009 \text{ kg m}^{-3}$; 0.9% excess density) near the basin floor ($h_i = 0.005 \text{ m}$). The density currents at 3 m downstream from the channel mouth along the basin centreline are demonstrated to be density-stratified (cf. Stacey and Bowen, 1988) throughout the experimental run: the density time-series plot for the flow current at this position (**Fig. 3H**) exhibits a distinct dense region near the basal part of the flow and a dilute region at the upper part of the flow.

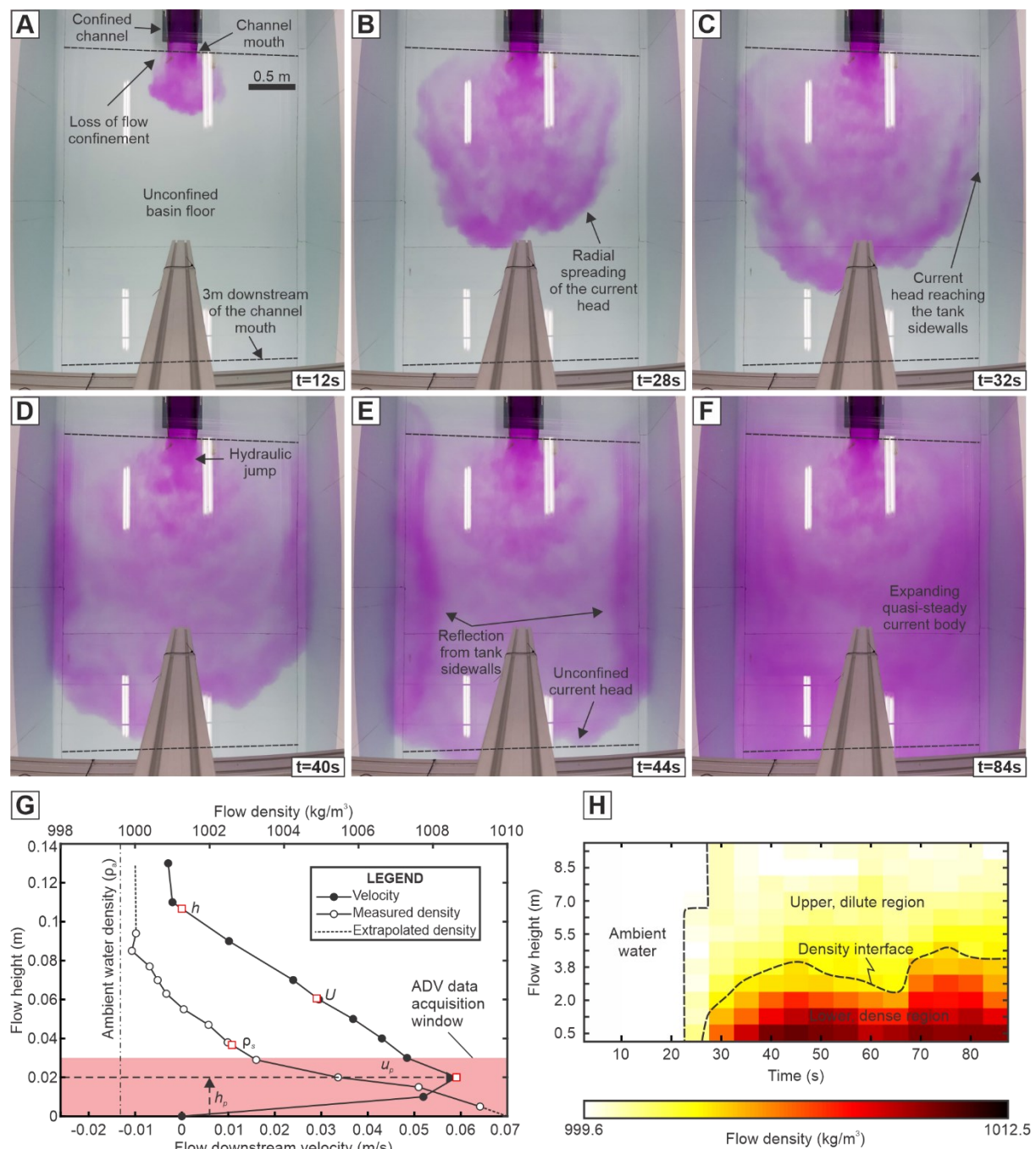


Fig. 3. (A-F) Set of overhead photographs illustrating the evolution of the saline density currents from the channel section to the basin floor in the unconfined reference experiment. Note that a radial hydraulic jump was observed immediately downstream of the channel mouth. (G) Profiles of time-averaged flow downstream velocity and density for the experimental density current recorded at 3 m downstream of the channel mouth along the channel-basin centreline in the unconfined reference experiment. Both measurements were initiated 5 s after

the current head passed and lasted for 30 s. The flow depth h , maximum downstream velocity u_p , its height above the basin floor h_p , depth-averaged downstream velocity U and depth-averaged density ρ_s are shown in the panel as red squares. The ambient water density was measured at 12°C. (H) Time-series profiles of flow density measured at 3 m downstream of the channel mouth along the channel-basin centreline, the position of which is shown as a red circle in **Figure 1A**.

Interaction of turbidity currents with containing topography in the ramp experiments

General flow behaviour

Here, experimental observations for Experiment S20°IN75° (**Fig. 4**) are described in detail to summarize the general flow behaviour when flows encounter the topographic slope. Once the flow exits the channel, it propagates along the basin as an unconfined underflow until encountering the containing slope (**Fig. 4A**). Upon incidence with the topographic slope, the flow decelerates and becomes strongly multidirectional on the slope surface (**Fig. 4B**). Simultaneously, flow stratification promotes the original flow to be decoupled into two parts: a lower denser part, and an upper less dense part. The dilute upper part of the flow runs up the slope surface and thins until reaching its maximum height H_{max} ('maximum run-up height', hereafter; cf. Pantin and Leeder, 1987; Edwards et al., 1994; **Fig. 4C**). This is termed as flow thinning and stripping on the slope surface hereafter. In contrast, the dense, lower part of the flow collapses back down the slope and is either deflected parallel to the slope and/or reflected towards the inlet at the base of the slope (**Fig. 4C**). The zone of flow stripping on the slope surface can be quantified by the height of the initial reversal of the dense lower flow H_{min} and the maximum run-up height H_{max} . Specifically, the lower limit of the flow stripping zone is quantified by the height upslope at which the basal region of the flow reverses downslope because this marks the onset of flow thinning upslope. The initial reversal of the dense lower

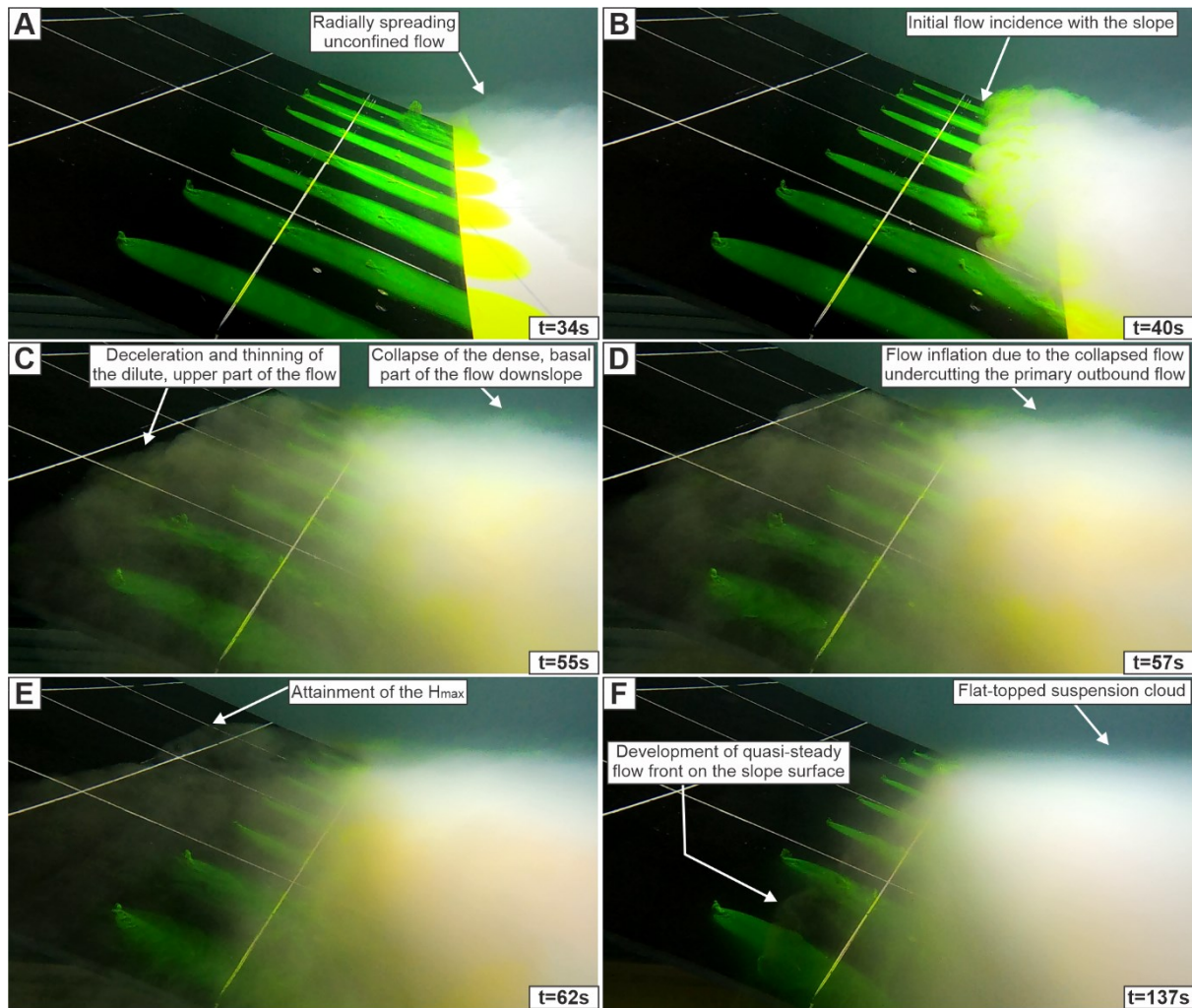


Fig. 4. Representative side-view photographs depicting the temporal evolution of density currents upon incidence with an oblique topographic slope (Experiment S20°IN75° for example). H_{max} denotes the maximum height that the dilute, upper part of the flow can run up on the slope surface. t denotes the experimental time since the release of the flow from the mixing tank.

part of the flow can undercut the primary outbound flow and migrate upstream from the slope before eventually dissipating in the basin. This initial flow reversal of the basal part of the flow just above the containing slope leads to a thickening of the entire body of the density current (Fig. 4D), which is termed as an unsteady ‘inflation’ phase of the suspension cloud by Patacci

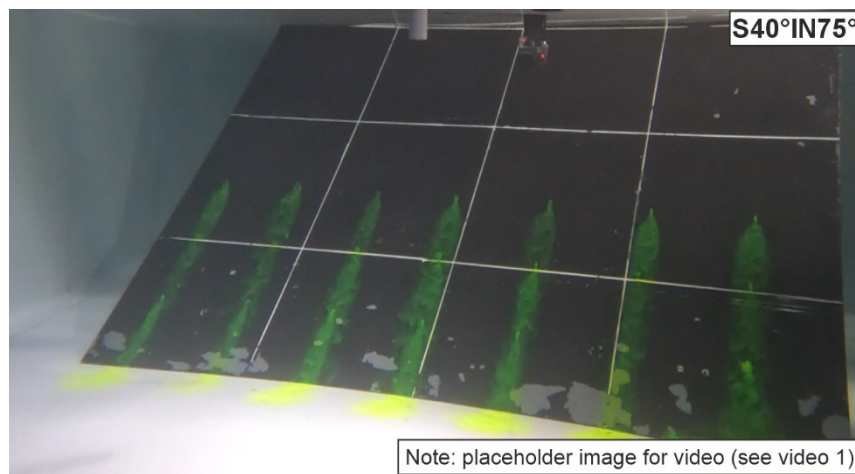
et al. (2015). Subsequently, as the parental flow re-establishes, the suspension cloud in the basin becomes flat-topped (i.e., a sharp, subhorizontal interface with the ambient water) and a quasi-stable flow front develops on the slope surface (**Fig. 4F**). This is termed a quasi-steady phase by Patacci et al. (2015). Finally, the waning of the inlet flow causes the suspension cloud to collapse. Note that no trains of upstream-migrating solitons or bores are observed throughout the experiments (cf. Pantin and Leeder, 1987; Edwards et al., 1994). Flow behaviour, including the degree of lateral flow expansion on the slope surface, the degree of flow thinning and stripping, and the relative strength between flow deflection and reflection, varies as a function of both the slope gradient and the incidence angle of the flow onto the slope.

Variation of incidence angles of the current onto the slope

The effects of containing slope orientation, with respect to flow direction, on flow behaviour were explored by systematically changing the incidence angles of the flow to the slope with the same slope gradient. Here, the results for 3 of the 18 experiments are presented: S40°IN75°, S40°IN60° and S40°IN15° (**Videos 1-3**).

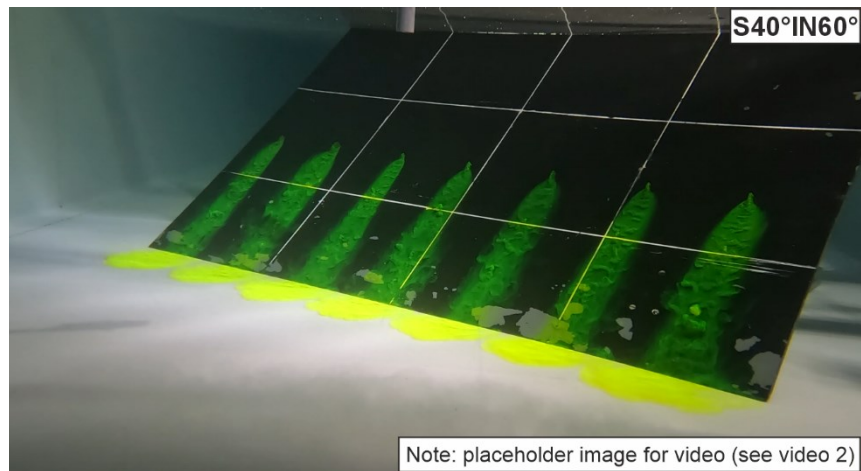
In Experiment S40°IN75° (**Video 1**), upon encountering the topographic slope, the flow runs into the slope strongly and results in a wide divergence in flow velocity directions on the slope surface. The area of lateral flow expansion on the slope surface is the largest among the three experiments. The maximum run-up height ($H_{max} = 0.29$ m) occurs in the middle of the ramp, whereas the height of initial flow reversal develops at ca. 0.13 m. Due to the high degree of topographic containment generated by the oblique ramp orientation in this experiment, reflection of the dense, basal part of the current is the strongest among these three experiments. Part of the dense, basal part of the flow is deflected and runs parallel to the slope. This basal flow is diverted at the point of incidence to the slope into two directions towards the lateral

edges of the slope, with the dividing streamline or plane (cf. Kneller and McCaffrey, 1999) at ca. 0.56 m from the right edge of the ramp.



Video 1. Annotated video illustrating the behaviour of density currents upon incidence with an oblique topographic slope (Experiment S40°IN75°).

In Experiment S40°IN60° (**Video 2**), relatively less flow is observed to be able to run up the slope and more of the flow is deflected towards the lateral edge of the slope, compared to Experiment S40°IN75°. The divergence in flow velocity directions on the slope surface is also less pronounced. The area of lateral flow expansion on the slope surface decreases markedly. H_{max} develops at the right edge of the ramp, at ca. 0.24 m upslope; the height of initial flow reversal is 0.13 m upslope. Flow reflection at the basal part of the slope is less pronounced due to a decrease in the topographic containment (see also *Temporal velocity pulsing* subsection). Hence, basal flow deflection is stronger relative to flow reflection, in contrast to Experiment S40°IN75°. The dividing streamline of the deflected dense, basal region of the flow is ca. 0.37 m from the right edge of the ramp.

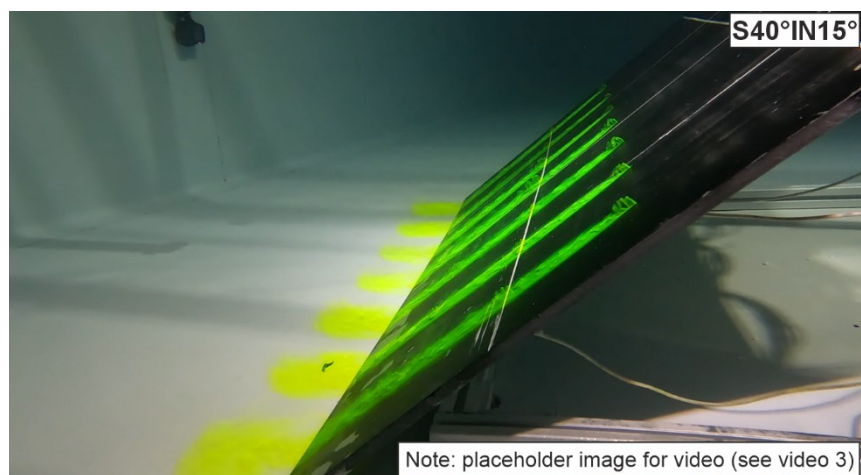


435

436 Video 2. Annotated video illustrating the behaviour of density currents upon incidence with an
437 oblique topographic slope (S40°IN60°).

438

439 In Experiment S40°IN15° (**Video 3**), the highly oblique ramp orientation results in the current
440 mainly being deflected parallel to the base of the slope with extremely limited interaction
441 between the current and slope surface (i.e., limited flow reflection or lateral flow expansion).
442 The zone of flow thinning and stripping on the slope surface is negligible, with the height of
443 initial flow reversal located at 0.12 m upslope and maximum run-up height at 0.16 m upslope.



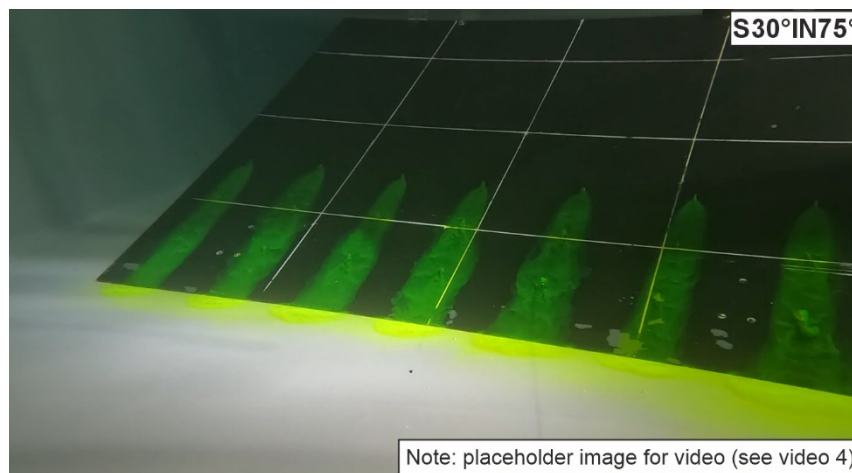
444

445 Video 3. Annotated video illustrating the behaviour of density currents upon incidence with an
446 oblique topographic slope (Experiment S40°IN15°).

447

Variation of slope gradients

The effects of slope gradient on flow behaviour were investigated using a single oblique incidence angle. Here, the results for 3 of the 18 ramp experiments are presented: S20°IN75°, S30°IN75° and S40°IN75° (**Fig. 4, Videos 1 and 4**).



Video 4. Annotated video illustrating the behaviour of density currents upon incidence with an oblique topographic slope (Experiment S30°IN75°).

Results in Experiment S40°IN75° were described in the preceding section. In Experiment S30°IN75° (**Video 4**), upon encountering the containing slope, the flow strikes the slope less strongly and becomes multidirectional on the slope surface but with a much larger area of lateral flow expansion, compared to Experiment S40°IN75°. H_{max} occurs laterally at ca. 0.37 m away from the right edge of the ramp, and ca. 0.36 m upslope; the height of initial flow reversal is ca. 0.12 m upslope. The strength of the flow reflection is not apparent in the visualisation video. However, the deflection of the dense, basal part of the flow can be identified. The basal flow is deflected into two directions towards the two lateral edges of the slope, respectively, with the dividing streamline ca. 0.56 m from the right edge of the ramp.

In Experiment S20°IN75° (**Fig. 4**), a much larger area of lateral flow expansion on the slope surface is observed, compared to former experiments. H_{max} occurs laterally at ca. 0.37 m away from the right edge of the ramp, and ca. 0.26 m upslope; the height of initial flow reversal is ca. 0.1 m upslope. Like the case in Experiment S30°IN75°, the strength of flow reflection cannot be identified visually, but part of the basal flow is deflected to run parallel to the slope.

Temporal velocity pulsing

From the flow visualisation videos, a series of upstream-migrating velocity reversals in the basal part of the flow can be identified, above the flat basin floor near the base of slope, and on the slope surface (**Videos 1-4**). Furthermore, the depth-constrained ADV down-dip velocity time-series profiles (**Figs 5-8**) capture the velocity reversals quantitatively at a point.

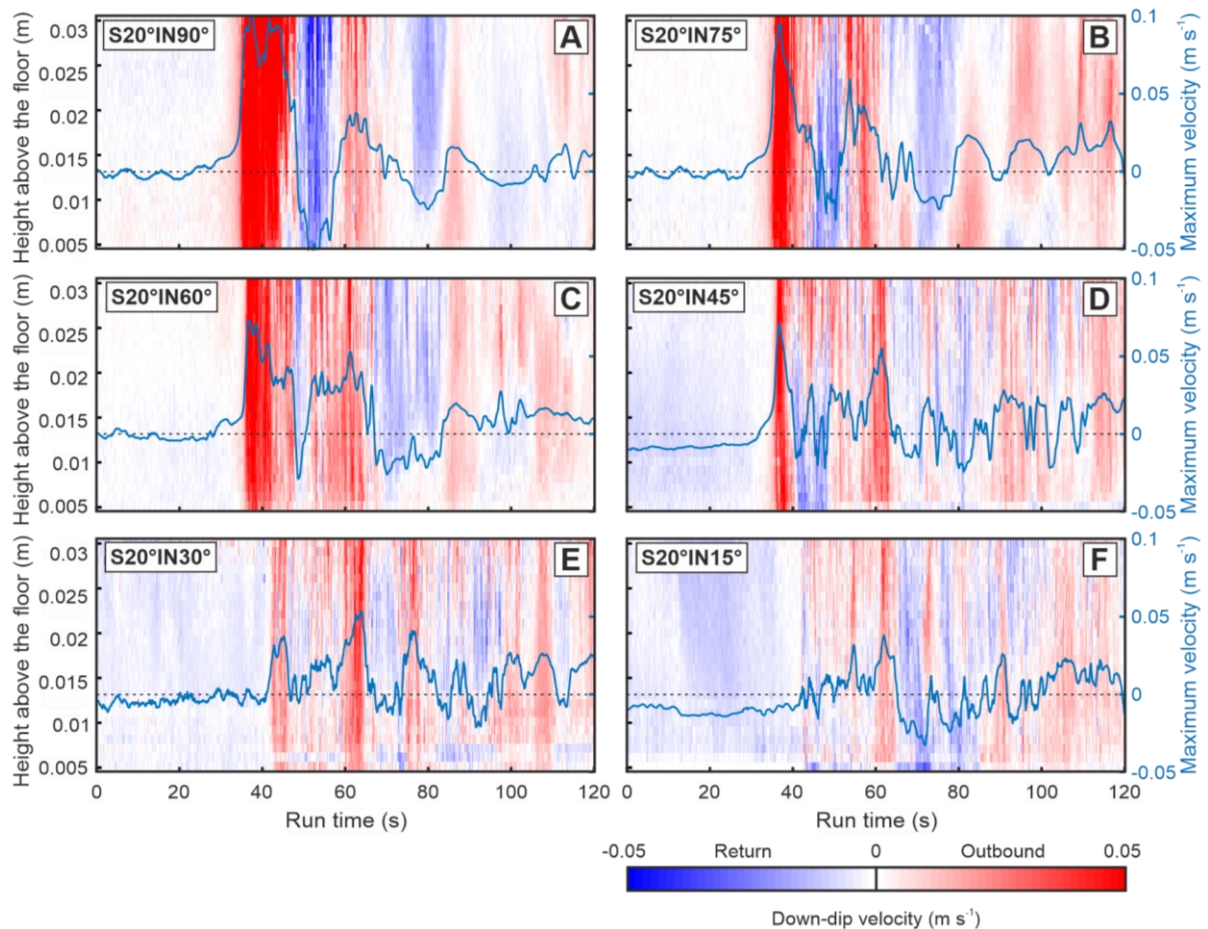


Fig. 5. Down-dip velocity time series of the density currents recorded at the base of the slope along the channel-basin centreline (ADV1 in Figure 1) for the ramp experiments (i.e., S20°IN90°, S20°IN75°, S20°IN60°, S20°IN45°, S20°IN30° and S20°IN15°). For visualisation, the data are clipped at $z \sim 0.5$ cm due to excess noise, caused by reflections. The temporal evolution of maximum velocity up/down the ramp, U_{max} , [i.e., the highest value over the measured height range (0.7-3.0 cm) of the ADV profiles] is also shown (blue solid lines).

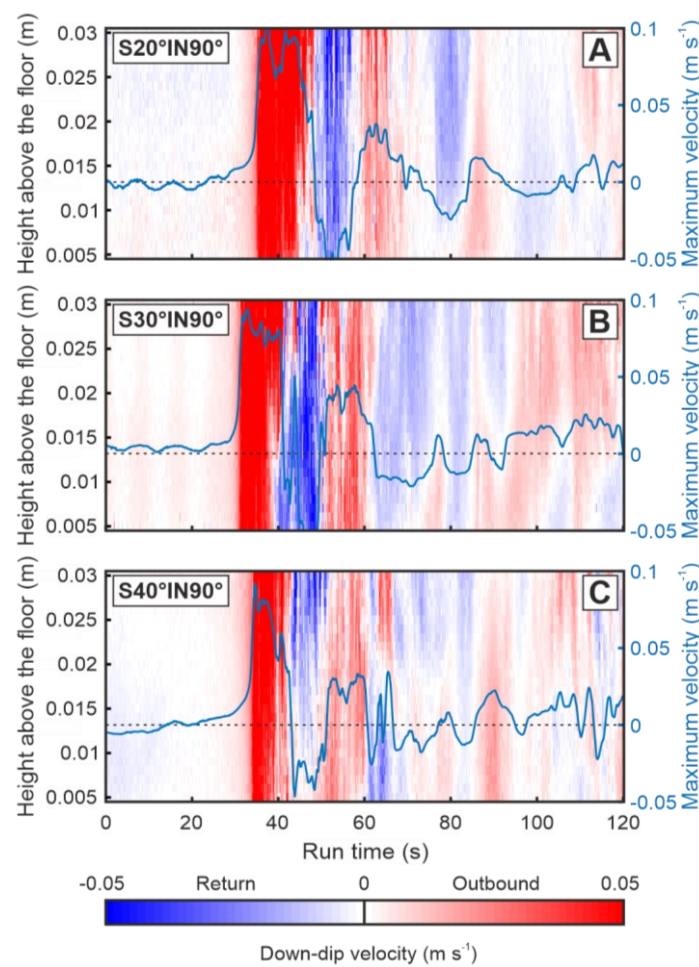


Fig. 6. Down-dip velocity time series of the density currents recorded at the base of the slope along the channel-basin centreline (ADV1 in Figure 1) for the ramp experiments (i.e., S20°IN90°, S30°IN90° and S40°IN90°). For visualisation, the data are clipped at $z \sim 0.5$ cm due to excess noise, caused by reflections. Positive values of the down-dip velocity depict flows

travelling towards the ramp, whereas negative values depict flows travelling away from the ramp and back towards the inlet. The temporal evolution of maximum velocity up/down the ramp, U_{max} , [i.e., the highest value over the measured height range (0.7-3.0 cm) of the ADV profiles] is also shown (blue solid lines).

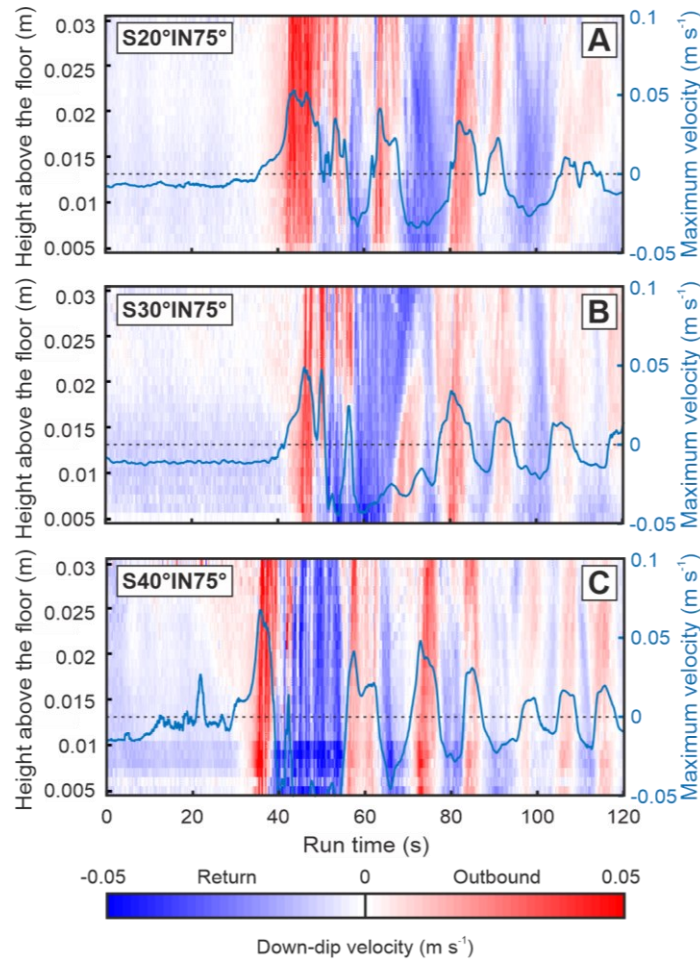


Fig. 7. Down-dip velocity time series of the density currents recorded at the flow front position just above the slope surface (ADV3 in Figure 1) for the ramp experiments (i.e., S20°IN75°, S30°IN75° and S40°IN75°). For visualisation, the data are clipped at $z \sim 0.5$ cm due to excess noise, caused by reflections. The temporal evolution of maximum velocity up/down the ramp, U_{max} , [i.e., the highest value over the measured height range (0.7-3.0 cm) of the ADV profiles] is also shown (blue solid lines).

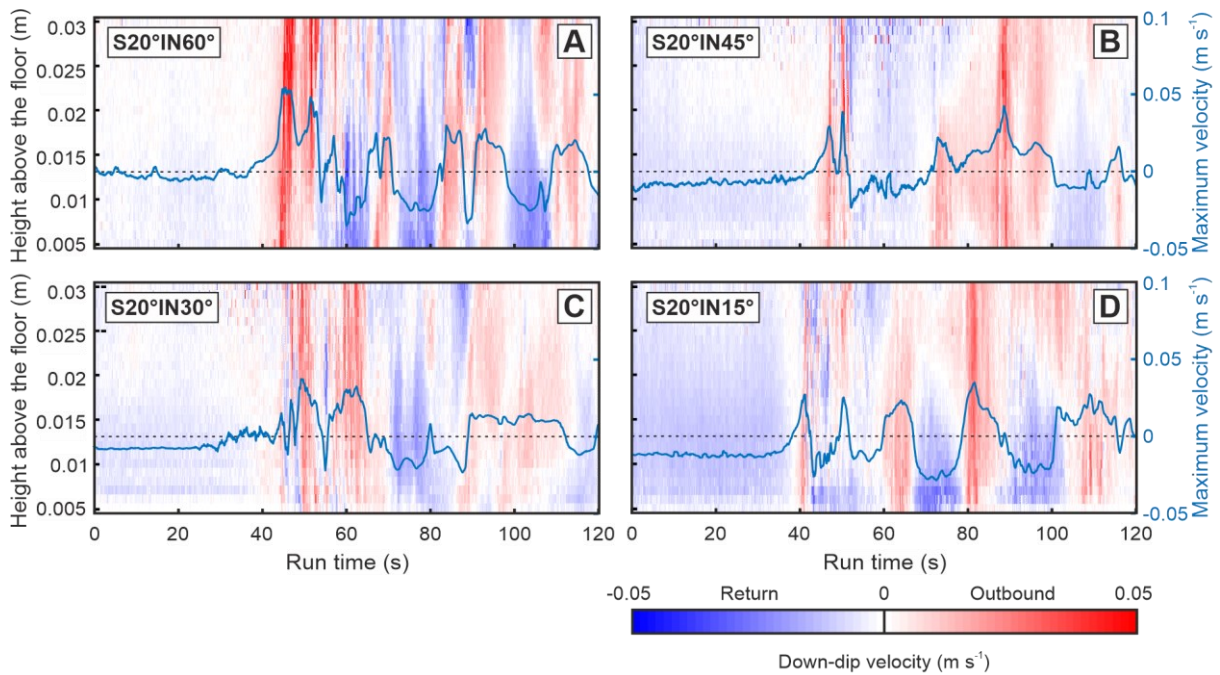


Fig. 8. Down-dip velocity time series of the density currents recorded at the flow front position just above the slope surface (ADV3 in Figure 1) for the ramp experiments (i.e., S20°IN60°, S20°IN45°, S20°IN30° and S20°IN15°). For visualisation, the data are clipped at $z \sim 0.5$ cm due to excess noise, caused by reflections. The temporal evolution of maximum velocity up/down the ramp, U_{max} , [i.e., the highest value over the measured height range (0.7-3.0 cm) of the ADV profiles] is also shown (blue solid lines).

Base of slope: Reflection and basal flow reversal

Down-dip velocity time-series profiles of the flow recorded near the base of slope along the channel-basin centreline (**Figs 5-6**) exhibit multiple basal flow reversals when the flow encounters the topographic slope. Notably, the first basal flow reversal is of high-velocity and highly turbulent, which is succeeded by a series of weaker basal flow reversals. After the first basal flow reversal diminishes, the second reversal typically re-establishes from an initially very low velocity to a final high velocity. The velocity of each reversal is generally lower than the preceding one. Nevertheless, the magnitude of the velocity, the number of velocity pulses,

and the duration of each pulse are different across the ramp experiments, as a function of both incidence angle and slope gradient.

Base of slope: Variation of incidence angles of the current onto the slope

Variation of incidence angle as a function of a single slope gradient (20°) is examined for experiments $S20^\circ IN90^\circ$, $S20^\circ IN75^\circ$, $S20^\circ IN60^\circ$, $S20^\circ IN45^\circ$, $S20^\circ IN30^\circ$ and $S20^\circ IN15^\circ$ (**Fig. 5**). Notably, for lower incidence angles, the magnitude of the maximum down-dip velocity U_{max} markedly decreases ($U_{max} = 0.06 \sim 0.008 \text{ m s}^{-1}$ for the basal flow reversals in Experiment $S20^\circ IN90^\circ$ and $U_{max} = 0.03 \sim 0.01 \text{ m s}^{-1}$ in Experiment $S20^\circ IN15^\circ$). Furthermore, the velocity pattern tends to be characterised by more pulses ($N = 3$ for the basal flow reversals in Experiment $S20^\circ IN90^\circ$ and $N > 7$ in Experiment $S20^\circ IN15^\circ$) and shorter time duration of each pulse ($T = 8 \sim 12 \text{ s}$ for the basal flow reversals in Experiment $S20^\circ IN90^\circ$ and $T = 2 \sim 7 \text{ s}$ in Experiment $S20^\circ IN15^\circ$).

Base of slope: Variation of slope gradients

For cases across different slope gradients, results of the experiments $S20^\circ IN90^\circ$, $S30^\circ IN90^\circ$ and $S40^\circ IN90^\circ$ are presented (**Fig. 6**). In Experiment $S20^\circ IN90^\circ$ (**Fig. 6A**), the first basal flow reversal begins ca. 13 s after the arrival of the first outbound flow and subsequently sustains for ca. 10 s until the re-establishment of the second outbound flow. The maximum magnitude of the first velocity reversal reaches ca. 0.06 m s^{-1} . This is followed by four weaker flow reversals, with time duration of each pulse of 11, 12, 3, and 1.4 s respectively and U_{max} ranging from 0.005 to 0.026 m s^{-1} . In Experiment $S30^\circ IN90^\circ$ (**Fig. 6B**), the first basal flow reversal arrives at 9 s after the first outbound flow initially establishes, which then sustains for ca. 8 s with a recorded down-dip maximum velocity over height of 0.06 m s^{-1} . This is succeeded by three weaker flow reversals, with time duration of each pulse of 14, 6 and 4 s respectively and U_{max} ranging from 0.011 to 0.023 m s^{-1} . In Experiment $S40^\circ IN90^\circ$ (**Fig. 6C**), the first basal

flow reversal starts to develop at 10 s after the arrival of the first outbound flow, which then sustains for ca. 5.5 s with a recorded down-dip maximum velocity over height of 0.04 m s^{-1} . This is succeeded by seven weaker flow reversals, with time duration of each pulse of 4, 4.4, 6, 5, 3, 2 and 3 s respectively and U_{max} ranging from 0.008 to 0.026 m s^{-1} . For cases across different slope gradients, the magnitude of the maximum velocity shows minimal difference. However, experiments with a higher angle of slope gradient are demonstrated to be dominated by more velocity pulses and shorter time duration of each pulse.

In summary, the incidence angle of the current relative to the containing slope exerts a much stronger control on the velocity pulsing pattern of the flow near the base of the slope (e.g., the strength and time duration of each basal flow reversal) than the slope gradient.

On the slope: Flow front velocity fluctuation

During the quasi-steady phase of each ramp experiment, a quasi-stable flow front develops on the slope surface, which fluctuates over a short distance up slope (**Fig. 4F**). Fluctuations of the flow front velocity are examined quantitatively via the depth-constrained ADV down-dip velocity time-series profiles positioned at the centreline of the ramp (ADV3 in **Figure 1**; **Figs 7-8**). Compared to measurements located at the base of the slope, the velocity magnitude of the flow front is lower. The velocity structure, number of velocity pulses, and time duration of each pulse (**Figs 7-8**) are a function of both the incidence angle of the flow and the slope gradient.

For cases with different slope gradients ($S20^\circ IN75^\circ$, $S30^\circ IN75^\circ$ and $S40^\circ IN75^\circ$), the magnitude of the maximum down-dip velocity U_{max} exhibits only small variation, between - 0.05 and 0.07 m s^{-1} (**Fig. 7**). Experiments with a steeper slope gradient configuration are associated with relatively more velocity pulses and shorter time duration of each pulse albeit the differences are small.

Considering experiments S20°IN75°, S20°IN60°, S20°IN45°, S20°IN30° and S20°IN15°, those with a lower flow incidence angle tend to show comparatively fewer and longer duration velocity pulses (**Fig. 8**). The velocity pulse patterns are irregular, i.e., non-periodic. U_{max} does not vary markedly between cases with different incidence angle configurations. For example, $-0.035 \sim 0.05 \text{ m s}^{-1}$ in Experiment S20°IN75° and $-0.04 \sim 0.03 \text{ m s}^{-1}$ in Experiment S20°IN15°.

Temporal variability of flow direction at the near-bed region

Temporal variability of the flow velocity vector (based on streamwise and cross-stream velocity, i.e., projected in the horizontal basin-floor plane) of the current recorded at 0.01 m above the basin floor and/or the slope surface is examined for each ramp experiment (**Figs 9-12**). A specific height of 0.01 m was chosen, to avoid any possible noise-induced interference, whilst focusing on the near-bed velocity as this is critical for sediment transport and deposition processes.

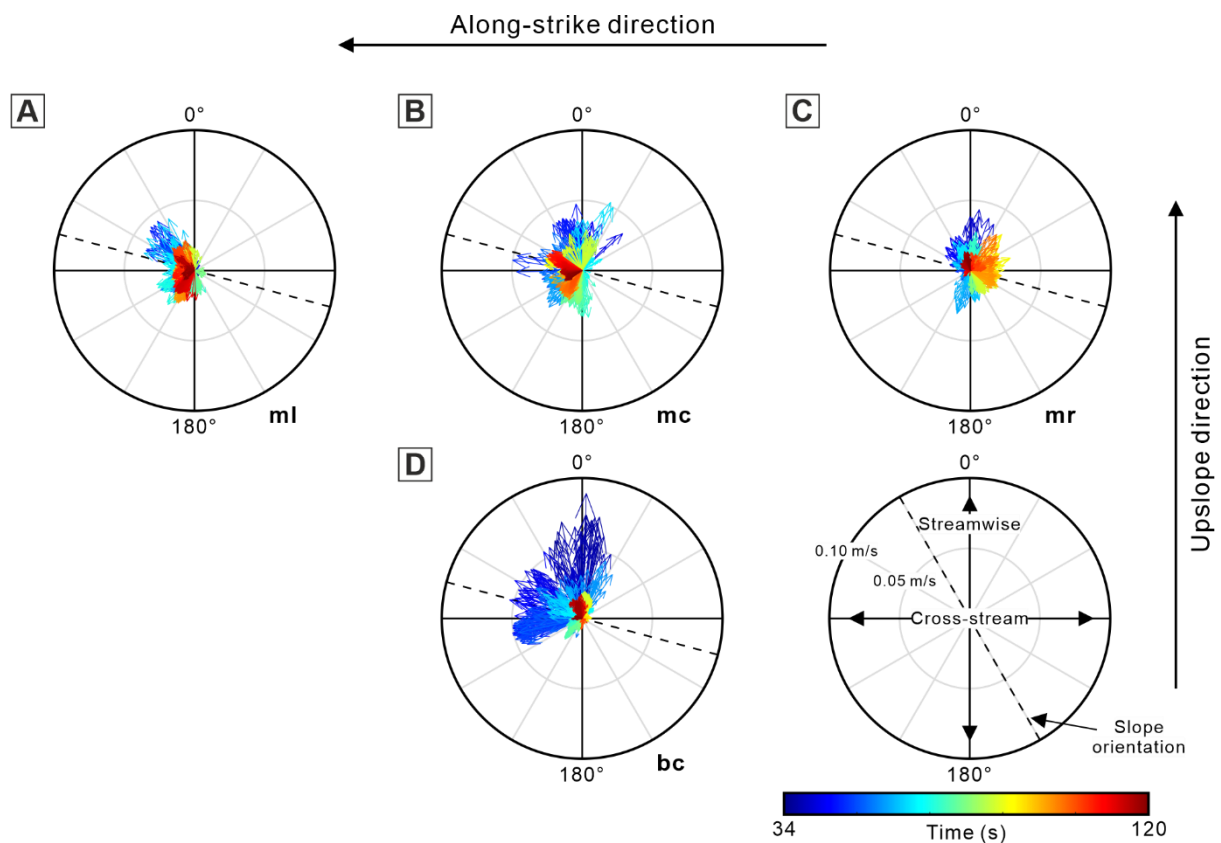


Fig. 9. Compass plots illustrating the spatial and temporal variability of the flow velocity vector (projected in the horizontal basin-floor) of the current within the quasi-steady phase (34 ~ 120 s) recorded at 0.01 m above the basin floor and/or the slope surface in Experiment S20°IN75°. ‘bc’ denotes the measurements at the base of slope along the channel-basin centreline and ‘ml’, ‘mc’ and ‘mr’ denote the measurements at the left, central and right flow front positions (in the flow direction), respectively (ADV4, ADV3 and ADV2 in **Figure 1**). In each compass plot, the arrow length denotes the velocity magnitude, and the direction denotes the velocity direction relative to the basin. Each arrow is colour coded as time. Black dashed line indicates the slope orientation. For presentation purposes, in each compass plot, the original 100 Hz ADV velocity data are decimated to 10 Hz.

Flow directions at the quasi-steady phase (34 ~ 120 s)

Measurements during the quasi-steady phase of the current (**Figs 9-11**) indicate that all ramp experimental configurations record complex patterns of flow direction and magnitude, including the presence of multidirectional combined flow regimes above the slope surface and near the base of slope.

For the ramp experiments (**Fig. 9**), flow velocity is higher at the base of slope than that at the flow front positions above the slope surface (e.g., maximum velocity of ca. 0.09 m s^{-1} vs. ca. 0.05 m s^{-1} in Experiment S20°IN75°). Current directions recorded at the flow front positions all exhibit a radial dispersal pattern whilst those recorded at the base of slope along the channel-basin centreline demonstrate diverse dispersal patterns including a radial dispersal and more unidirectional distribution pattern (**Figs 9-11**, see the descriptions below). In a single slope configuration (e.g., Experiment S20°IN75°), downstream current data above the slope typically

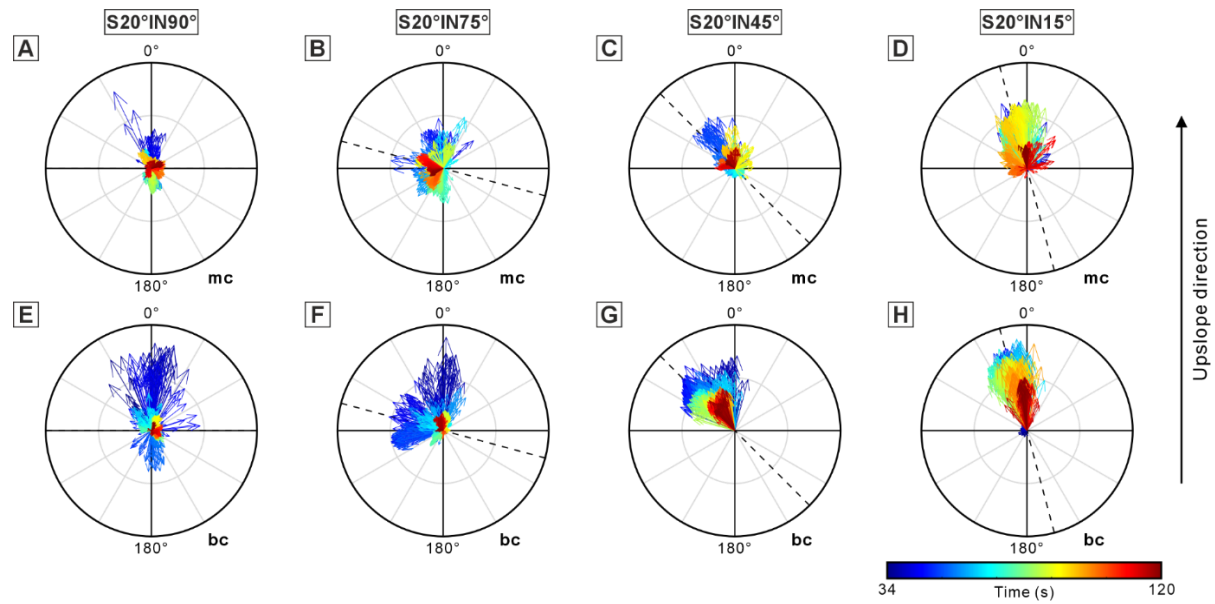


Fig. 10. Compass plots illustrating the temporal variability of the flow velocity vector (projected in the horizontal basin-floor) of the current recorded at 0.01 m above the basin floor and/or the slope surface within the quasi-steady phase (34 ~ 120 s) in Experiments S20°IN90° (A, E), S20°IN75° (B, F), S20°IN45° (C, G) and S20°IN15° (D, H). ‘bc’ denotes the measurements at the base of slope and ‘mc’ denotes the measurements at the central flow front position (ADV3 in **Figure 1**). In each compass plot, the arrow length denotes the velocity magnitude, and the direction denotes the velocity direction relative to the basin. Each arrow is colour coded as time. Black dashed line indicates the slope orientation. For presentation, in each compass plot, the original 100 Hz ADV velocity data are decimated to 10 Hz. See **Figure 9** for the legend of this figure.

show an increased unidirectional component in flow direction distribution, compared to those recorded upstream (reverse flow; e.g., **Fig. 9A, C**).

Across experiments with different flow incidence angles onto the slope (**Fig. 10**), base of slope flow directions show a gradual transition from a radial to a more unidirectional dispersal pattern (oriented to the along-strike direction parallel to the slope) as the flow incidence angle decreases (**Fig. 10E-H**; 0° ~ 360° in Experiment S20°IN90° vs. 320° ~ 30° clockwise in

Experiment S20°IN15°). On the slope, the unidirectional component of the flow recorded at the central flow front position increases with a lower incidence angle, although all configurations exhibit a radial dispersal pattern (**Fig. 10A-D**). However, the overall radial dispersal pattern above the slope surface is established in different ways. The flow direction in a highly oblique experimental configuration predominantly rotates with time, whereas in a less oblique experiment the flow velocity direction tends to maintain a radial pattern through time.

Across experiments with different slope gradients (**Fig. 11**), the velocity magnitude and the flow direction distribution do not vary markedly. Notably, with a steeper slope gradient, the velocity magnitude recorded at the base of slope or near the flow front tends to be slightly larger. Furthermore, for steeper slopes, typically the current data exhibit a slightly wider spread in both overall flow directions throughout the experiment (290° ~ 15° clockwise in Experiment S20°IN45° vs. 290° ~ 30° clockwise in Experiment S40°IN45°) and flow directions over a given period, compared to gentler topographic slopes.

In summary, the incidence angle of the current relative to the containing slope appears to influence the temporal variability of the flow direction at the near-bed region more strongly than the slope gradient. This holds true both for the flow at the base of slope and the flow front position along the channel-basin centreline.

637

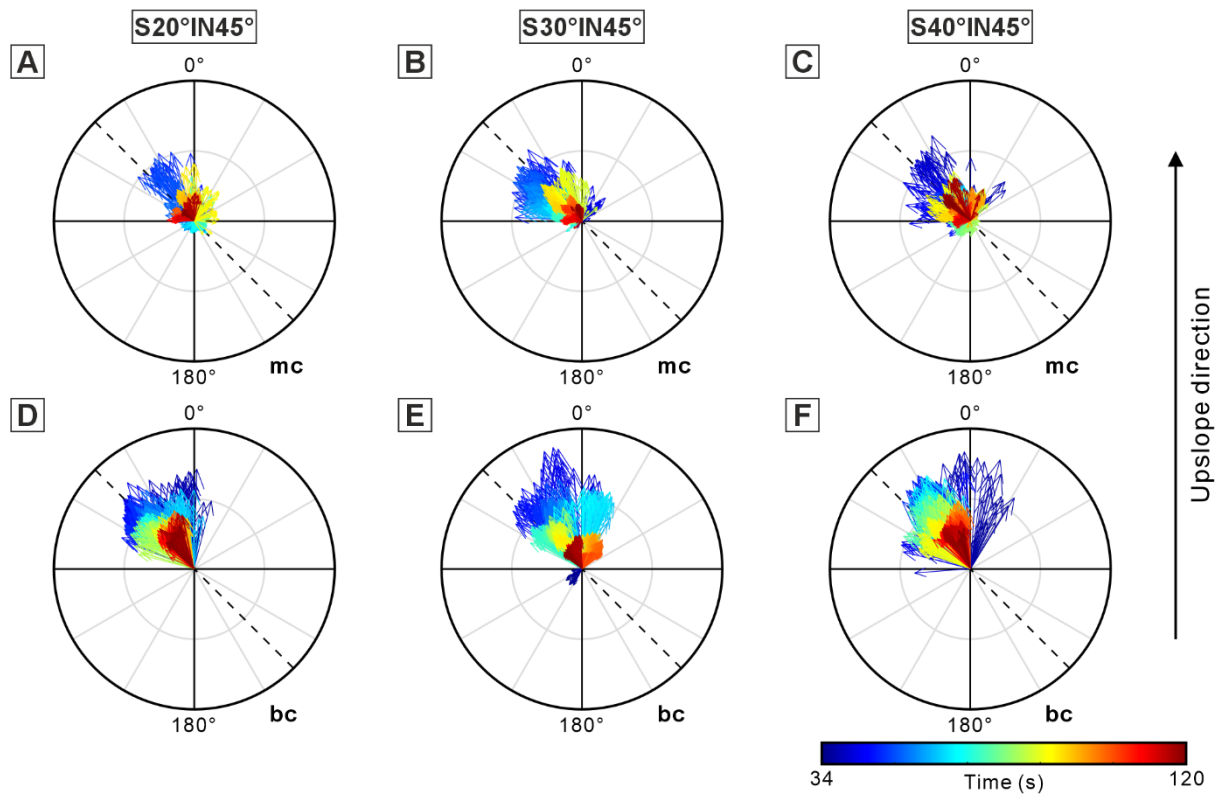


Fig. 11. Compass plots illustrating the temporal variability of the flow velocity vector (projected in the horizontal basin-floor) of the current within the quasi-steady phase (34 ~ 120 s) recorded at 0.01 m above the basin floor and/or the slope surface in Experiments S20°IN45° (A, D), S30°IN45° (B, E) and S40°IN45° (C, F). ‘bc’ denotes the measurements at the base of slope and ‘mc’ denotes the measurements at the central flow front position (ADV3 in **Figure 1**). In each compass plot, the arrow length denotes the velocity magnitude, and the direction denotes the velocity direction relative to the basin. Each arrow is colour coded as time. Black dashed line indicates the slope orientation. For presentation, in each compass plot, the original 100 Hz ADV velocity data are decimated to 10 Hz. See **Figure 9** for the legend of this figure.

Flow directions at the waning phase (160 ~ 180 s)

Temporal variability of the near-bed velocity vector above the slope surface during the waning phase of the current (**Fig. 12**) is analysed. This stage is critical for sediment deposition process,

652 especially the development of tractional bedforms such as ripples in the Bouma C division,
653 which in field studies are compared to sole structure orientation to interpret the presence and
654 orientation of seabed topography (e.g. Kneller et al., 1991; Hodgson and Haughton, 2004). This
655 specific time window (160 ~ 180 s), where velocities are about 10-20% of that of the quasi-
656 steady flow (**Fig. 12**), is chosen to avoid the later effects of reflections from the tank sidewalls.

657 Results indicate that within a near frontal experimental configuration (S20°IN75° and
658 S20°IN90°; **Fig. 12G-K**), the near-bed velocity vectors on the slope surface tend to be
659 dominated by a downslope flow direction with a nearly orthogonal angle to the topographic
660 slope orientation. This is likely because when the dilute flow declines higher up on the slope
661 surface, gravity starts to dominate and therefore the flow collapses orthogonal to the slope. In
662 a highly oblique or oblique experimental configuration (S20°IN15°; S20°IN45°; **Fig. 12A-F**),
663 the near-bed flow directions during the waning phase are more variable, with flows showing a
664 high degree of radial spreading in places (**Fig. 12B, 12E and 12F**), and mean flow angles in
665 the range of ~30-45° relative to the slope. This is attributed to the input flow not riding up the
666 slope as high, and therefore gravity has a minor influence relative to the basinward flow
667 momentum.

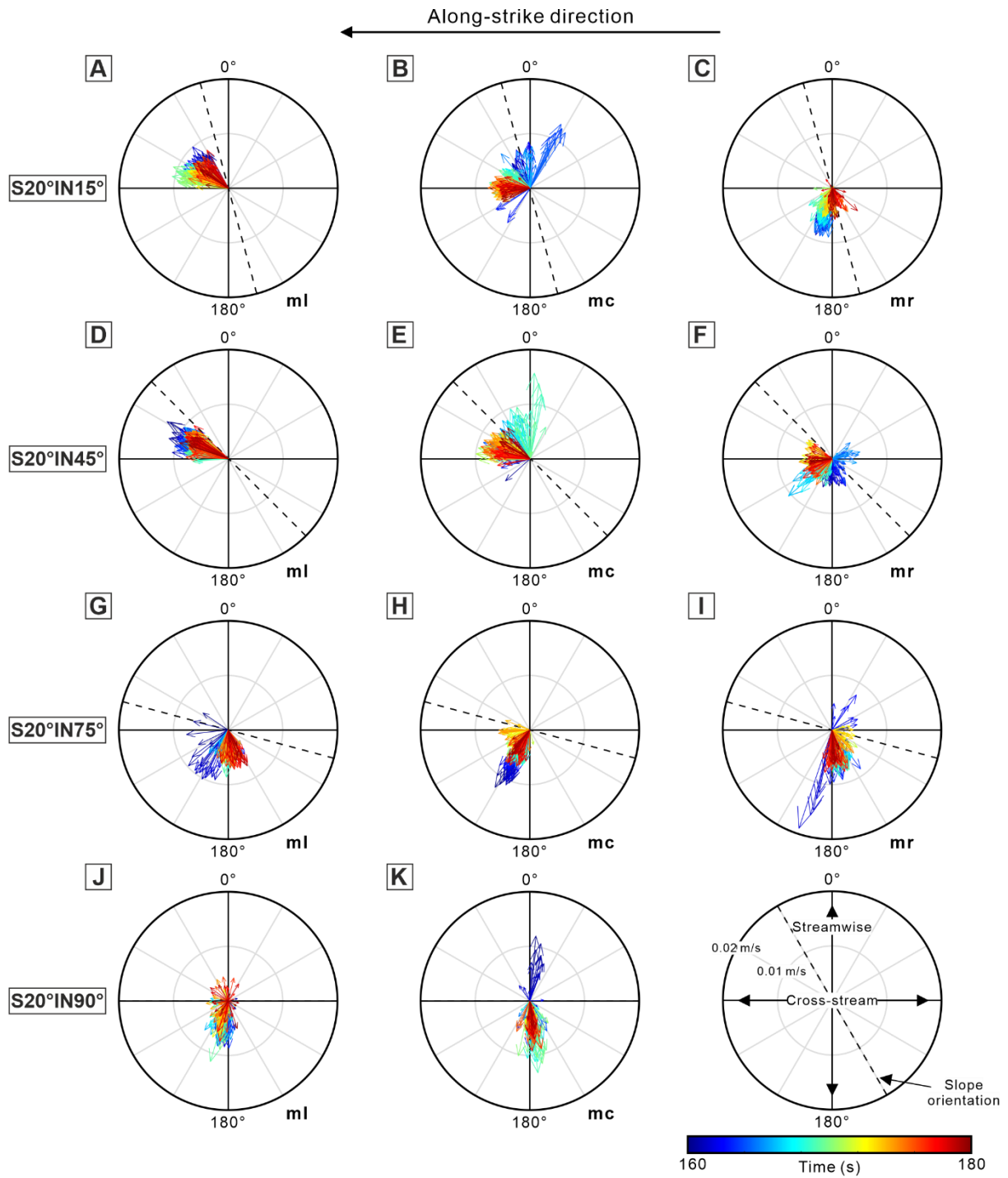


Fig. 12. Compass plots illustrating the temporal variability of the flow velocity vector (projected in the horizontal basin-floor) of the current within the waning phase (160 ~ 180 s) recorded at 0.01 m above the slope surface in Experiments S20°IN15° (A-C), S20°IN45° (D-F), S20°IN75° (G-I) and S20°IN90° (J, K). 'ml', 'mc' and 'mr' denote the measurements at the left, central and right flow front positions (in the flow direction), respectively (ADV4, ADV3

and ADV2 in **Figure 1**). In each compass plot, the arrow length denotes the velocity magnitude, and the direction denotes the velocity direction relative to the basin. Each arrow is colour coded as time. Black dashed line indicates the slope orientation. For presentation, in each compass plot, the original 100 Hz ADV velocity data are decimated to 10 Hz. Note the different velocity scale for the arrows relative to **Figures 9-11**.

DISCUSSION

Absence of internal waves in unconfined density current interactions with topographic slopes

In all the ramp experimental configurations, no well-defined internal wave-like features are observed (**Videos 1-4**), suggesting that features including solitons and bores do not develop above all of the planar topographic slopes. This is at odds with the presence of internal waves observed in previous narrow 2D flume tank (e.g., Pantin and Leeder, 1987; Edwards et al., 1994; Patacci et al., 2015) and qualitative 3D experiments (Kneller et al., 1991; Haughton, 1994; Kneller, 1995) when density currents encounter topographic slopes. The internal waves were either reflected bores or waves running along at the top of the density flow due to the reflection of the currents against topographic slopes (e.g., Pantin and Leeder, 1987; Edwards et al., 1994; Kneller et al., 1991) or linked to initial inlet properties of the flow such as Kelvin-Helmholtz instabilities (e.g., Patacci et al., 2015). The possible explanation for the absence of internal waves in this work is detailed in the following section.

Revisiting the paradigm of flow deflection and reflection

The prevailing paradigm for sediment gravity flow interaction with topographic slopes is that flow reflection is always orthogonal to the slope irrespective of the incidence angle of the flow

(Kneller et al., 1991; Kneller, 1995; Kneller and McCaffrey, 1999; **Fig. 13A**; note though that the single experiment in Houghton (1994) is slightly anomalous). This leads to a model where sole marks, representing basal conditions, can be at high angles to ripple directions, within the same bed; for flows parallel with containing topography, the angle is 90° (Kneller et al., 1991; Kneller, 1995; **Fig. 13B**). In turn, the reflections are linked to internal waves and/or solitons (Pantin and Leeder, 1987; Kneller et al., 1991; Edwards et al., 1994; Houghton, 1994; Kneller, 1995). However, the experiments herein do not support this model with a notable absence of downslope reflection at more oblique incident angles (15° and 45°) during the main body of the flow (**Figs 10 and 11, Video 3**), along with a lack of evidence for internal waves. In the present experiments the dominant flow processes transition from lateral divergence-dominated, through reflection-dominated, to deflection-dominated as the flow incidence angle varies from 90° - 15° and the slope gradient changes from 20° - 40° (**Fig. 14**).

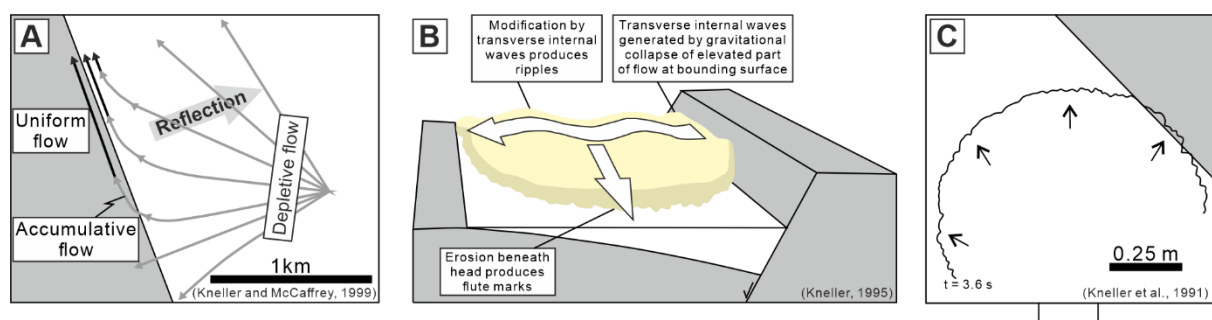


Fig. 13. Existing process models for flow deflection and reflection when sediment gravity flows encounter a topographic slope (A and B) and for the resulting relationship between sole mark and ripple directions (B). In these models, flow reflections are always orthogonal to the topographic slope, irrespective of the incidence angle of the flow against the slope. Ripples are formed as the product of internal waves travelling on the upper interface of the gravity current, as shown in (B). (C) Small-scale experiment of Kneller et al. (1991) as seen in planform, showing expanding flow interacting with a slope (marked in grey). Whilst the slope is oblique relative to the axial flow direction of the current, due to expansion the local flow direction is

orthogonal to the slope at the point where the flow interacts with the slope.

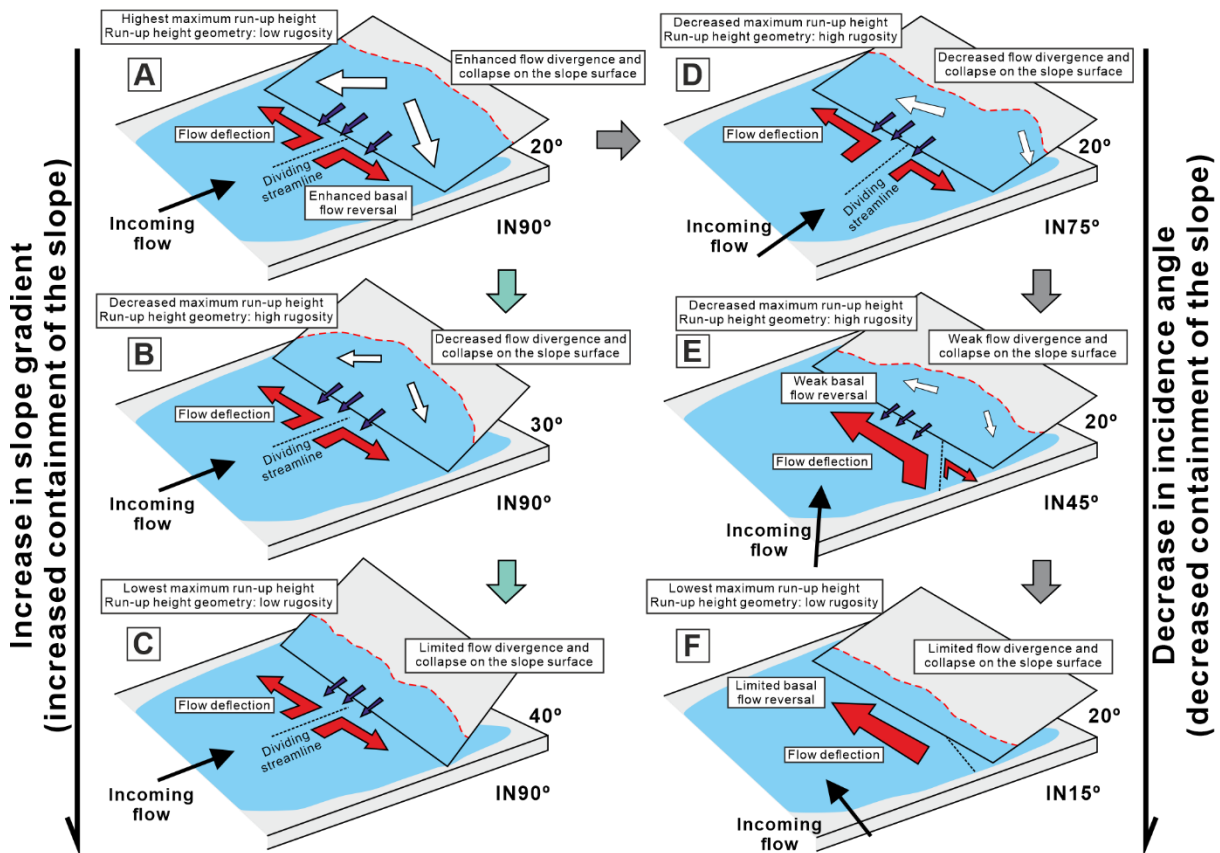


Fig. 14. Schematic diagram illustrating the influence of flow incidence angle onto the containing slope (A, D-F) and slope gradient (A-C) on the general flow behaviour.

The existing paradigm was developed from qualitative 3D experiments against oblique, and parallel to flow, containing slopes (Kneller et al., 1991; Kneller, 1995), which therefore appear paradoxical compared to the present experiments. The key to this conundrum is that the previous experiments were run in a very small tank, 1 m by 1 m in planform, and consequently flows were in a strongly expansional phase having exited the inlet channel when they interacted with the containing slope (Kneller et al., 1991, **Fig. 13C**). Hence, the local flow direction relative to the slope was approximately orthogonal (Kneller et al., 1991, **Fig. 13C**; Kneller,

1995, his fig. 13). Consequently, the slopes were not oblique relative to the local flow direction of the impinging flow, and therefore the resulting reflections were essentially orthogonal to the slope, and thus comparable with 2D experiments on orthogonal slopes (e.g., Edwards et al., 1994).

The previous 3D experiments (Kneller et al., 1991; Kneller, 1995) did generate clear internal waves, as also observed for 2D slopes (Edwards et al., 1994), which were not observed in the present experiments. Key to this difference may be the orders of magnitude differences in the density of the impinging flows. In the present study, flows were dilute ($\sim 0.3\%$ density difference), in contrast to $6.7\text{--}12.8\%$ density differences reported in Kneller et al. (1991), and 3% in Kneller (1995); note that these are initial values for the Kneller et al. (1991) and Kneller (1995) cases, however the small tank size limited the time for entrainment and dilution prior to impacting the slope. Flows that are 1-2 orders of magnitude greater in density will be prone to far stronger flow reflection, and will lack the run-up heights and more complex interaction with slopes observed herein. Whilst the bulk flow density of natural turbidity currents remains poorly known, the best estimates range from $<0.1\%$ to $\sim 0.2\%$ (Konsoer et al., 2013; Simmons et al., 2020), comparable to natural saline-driven density currents ($\sim 0.1\text{--}0.2\%$; Sumner et al., 2014; Azpiroz-Zabala et al., 2024). Consequently, the present experiments are far more comparable to those estimated from natural systems. However, this comparative exercise does suggest that flow density is a key variable that requires further assessment.

The model of ripple formation from internal waves is itself problematic. This is because the internal waves are postulated to form at the upper interface of the turbidity current (Kneller et al., 1991; Kneller, 1995). Given that natural unconfined or partially confined turbidity currents can be metres to tens of metres in thickness (e.g., Stevenson et al., 2013; Lintern et al., 2016; Hill and Lintern, 2022), it is unclear if the internal waves are able to penetrate to the bed. Furthermore, the internal wave driven model of Kneller (1995; **Fig. 13B**) has both the axial

757 flow and the ripple generating transverse flows present at the same time. However, there is a
758 temporal gap between the formation of the sole marks and the ripples, particularly as there may
759 be a substantial time gap between the cutting of the sole marks and the deposition of the
760 immediately overlying sediment (Peakall et al., 2020; Baas et al., 2021). Furthermore, the
761 ripples in the Bouma C division are typically formed right at the end of sand deposition. Thus,
762 it could be hypothesised that the ripples may reflect the waning phase of the flow where the
763 incident flow declines, leaving gravity to dominate, with flows collapsing orthogonal to the
764 slope. For high incidence angle slopes (75° and 90°) the present experiments show that waning
765 flows on slopes are orthogonal (**Fig. 12G-K**). In contrast, highly oblique slopes (15°) and
766 oblique slopes (45°) show far greater variability in flow directions in the waning flows (**Fig.**
767 **12A-F**), with flows showing a high degree of radial spreading in places (**Fig. 12B**), and mean
768 flow angles in the range of ~ 30 - 45° relative to the slope, rather than orthogonal (**Fig. 12A-C**).
769 So even waning flows in highly oblique systems are not predominantly orthogonal to slopes as
770 suggested in the existing model (Kneller et al., 1991; Kneller, 1995; Kneller and McCaffrey,
771 1999).

772 A further conundrum is that palaeocurrent data in elongate basins typically show high angles
773 between basin axial sole structures and basin transverse ripples in flows that were postulated
774 to be broadly parallel to slopes (e.g., Cope, 1959; Craig and Walton, 1962; Prentice, 1962;
775 Kelling, 1964; Seilacher and Meischner, 1965; Scott, 1967; Kneller et al., 1991; Smith and
776 Anketell, 1992), with Kneller et al. (1991) showing a peak in angular discordance between 60°
777 and 90° . These field data are thus in agreement with the Kneller et al. (1991) model of
778 orthogonal reflection. Given, the experiments herein demonstrate that orthogonal reflection is
779 not universal, as previously postulated (Kneller et al., 1991), and does not occur under highly
780 oblique incidence angles, why do flow parallel field examples appear to show orthogonal flow
781 reflection? In order to address this enigma, a flow visualisation experiment was undertaken of

782 a flow travelling parallel to a topographic ramp (**Fig. 15**). The visualisation (see **Fig. 15** and
783 **Video 5**) shows that a flow that is parallel to a planar bounding surface produces a series of
784 flow fronts that move up and down the topographic ramp. Given that the incidence angle is 0° ,
785 the flow collapses down the slope purely under gravity forcing, and thus moves orthogonal to
786 the slope. These orthogonal flows on the slope thus explain the field data from elongate basin-
787 fills.

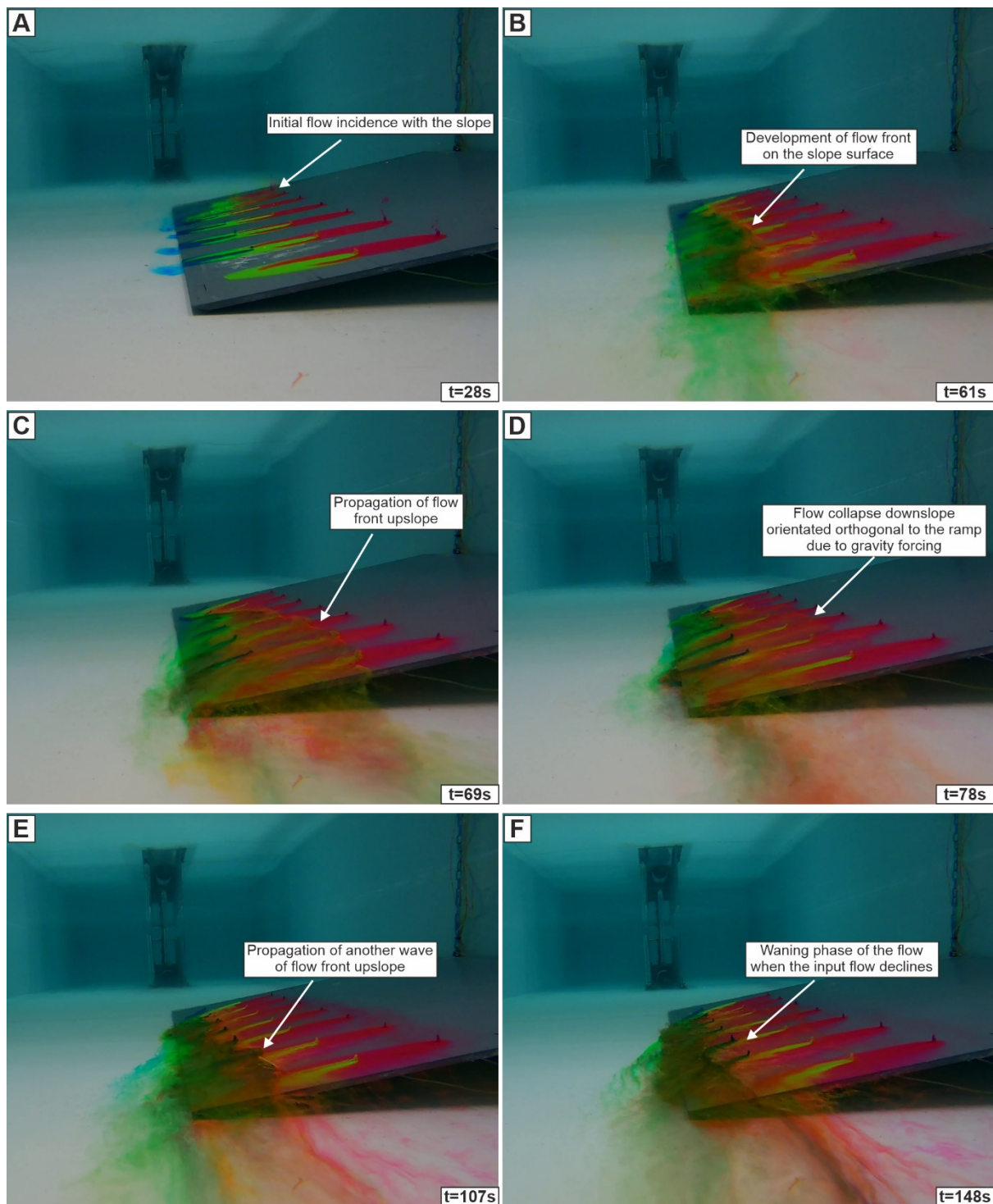
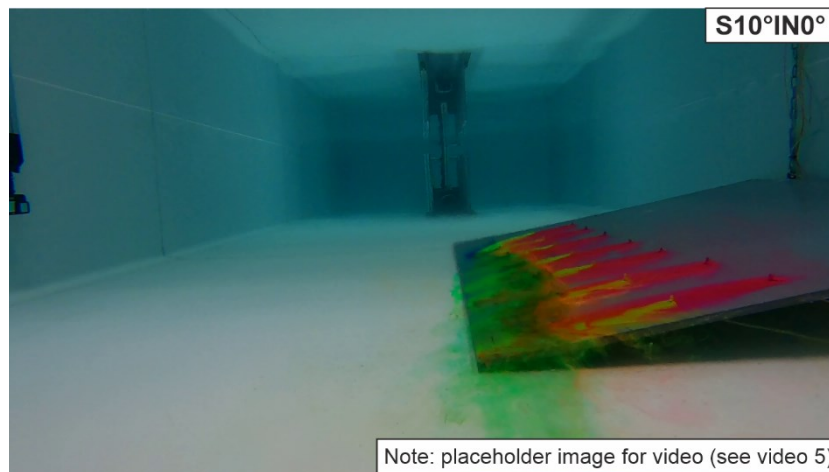


Fig. 15. Example images looking upstream depicting the temporal evolution of density currents upon incidence with a flow-parallel topographic slope of 10° slope gradient. t denotes the experimental time since the release of the flow from the mixing tank. Dye injection on the slope is used to visualise the flow behaviour. Note the repeated flow-front growth and collapse above the topographic slope moving in an orthogonal direction to the slope, with localised rugosity

along the flow front (also see Video 5 for more detail of this flow behaviour).



Video 5. Annotated video illustrating the behaviour of density currents upon incidence with a flow-parallel topographic slope of 10° slope gradient.

In summary, flows that are at very high angles to topographic slopes, produce orthogonal reflections down the slope. As flows become more oblique, they are deflected rather than reflected, and do not exhibit orthogonal reflections, even in the case of waning flows that might be expected to generate ripples. Once flows become parallel to topographic slopes (incidence angle of 0°), however, they exhibit flow-front growth and collapse on their flank against the bounding topographic slope. The collapsing flows on the flank thus are driven purely by gravity and show orthogonal flow directions relative to the slope, in agreement with the palaeocurrent data from elongate basin-fills. This new model of flow reflection, and deflection (**Fig. 16A; Fig. 14**), shows that the incidence angle of the flow against the slope is critical. Flows do not universally reflect orthogonally as believed for the past three decades (Kneller et al., 1991; Kneller and McCaffrey, 1999). The mechanics observed herein, are also radically different to that proposed in the current paradigm. Ripples are formed on slopes, and close to the base of slopes, by flows moving down the slope, in many cases during the waning of flows, rather than

being the product of internal waves travelling on the upper interface of the gravity current (Kneller et al., 1991; Kneller, 1995; **Fig. 16A-D**). The present model suggests that palaeocurrents showing high angles between sole marks and ripples, are formed on, or close to, slopes in contrast to the model of Kneller (1995; **Fig. 13B**) that shows such relationships occurring across entire basins.

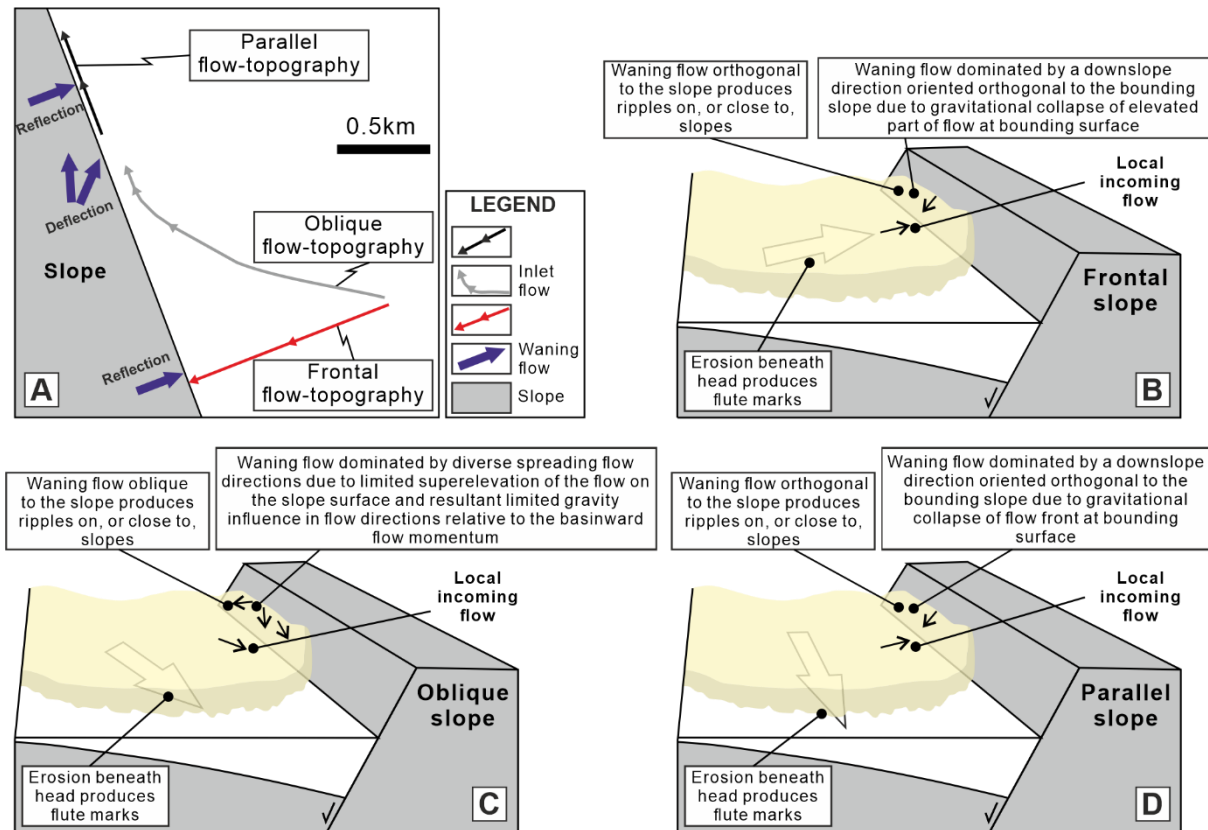


Fig. 16. A new process model proposed in this work highlighting the importance of incidence angle of the flow against the slope, on flow reflection and deflection. Flows that are at very high angles to topographic slopes (A and B), produce orthogonal reflections down the slope. As flows become more oblique (A and C), they are deflected rather than reflected, and do not exhibit orthogonal reflections, even in the case of waning flows that might be expected to generate ripples. Once flows become parallel to topographic slopes (incidence angle of 0° ; A and D), however, they exhibit flow-front growth and collapse on their flank against the bounding topographic slope. The collapsing flows on the flank thus are driven purely by gravity

and show orthogonal flow directions relative to the slope. In (B-D), ripples are formed on slopes, and close to the base of slopes, by flows moving down the slope, in many cases during the waning of flows, rather than being the product of internal waves travelling on the upper interface of the gravity current, as shown in **Figure 13B**.

Velocity pulsation on slopes

The input flow in the experiments is quasi-steady in nature (**Table 1**). However, distinct temporal velocity pulsing, or velocity unsteadiness, in the basal part of the flows is recorded in all experimental configurations, both at the base of, and on the topographic slope, as measured along the channel-basin centreline (**Figs 5-8**). This velocity pulsing is generated by the repeated fluctuations of the flow front, with periodic collapses of fluid down the slope. In turn, the nature of the velocity pulsing in terms of velocity amplitude and frequency varies as a function of incidence angle and slope angle; see **Fig. 17** for a schematic illustration of these variations. This mechanism for velocity pulsing is therefore tied to slopes and the base of slopes, but will likely not propagate much farther into the basin. Slopes have previously been associated with the generation of velocity pulsing, but this has either been in the form of solitons and internal waves (Kneller et al., 1991, 1997; Edwards et al., 1994; Kneller, 1995; Patacci et al., 2015), or the generation of true oscillatory flows has been postulated (Tinterri, 2011; Tinterri and Muzzi Magalhaes, 2011). The present experiments do not show any evidence for the generation of oscillatory flows, with the pulsation related to movement of fluid up and down the slope, rather than propagation of a wave through the medium. Similarly, there is no evidence for solitons or internal waves in the present experiments. The three-dimensional nature of the present experiments and flow density values that are orders of magnitude lower than some previous experiments and more commensurate with those of natural flows, likely account for the absence of these solitons and internal waves, as discussed previously.

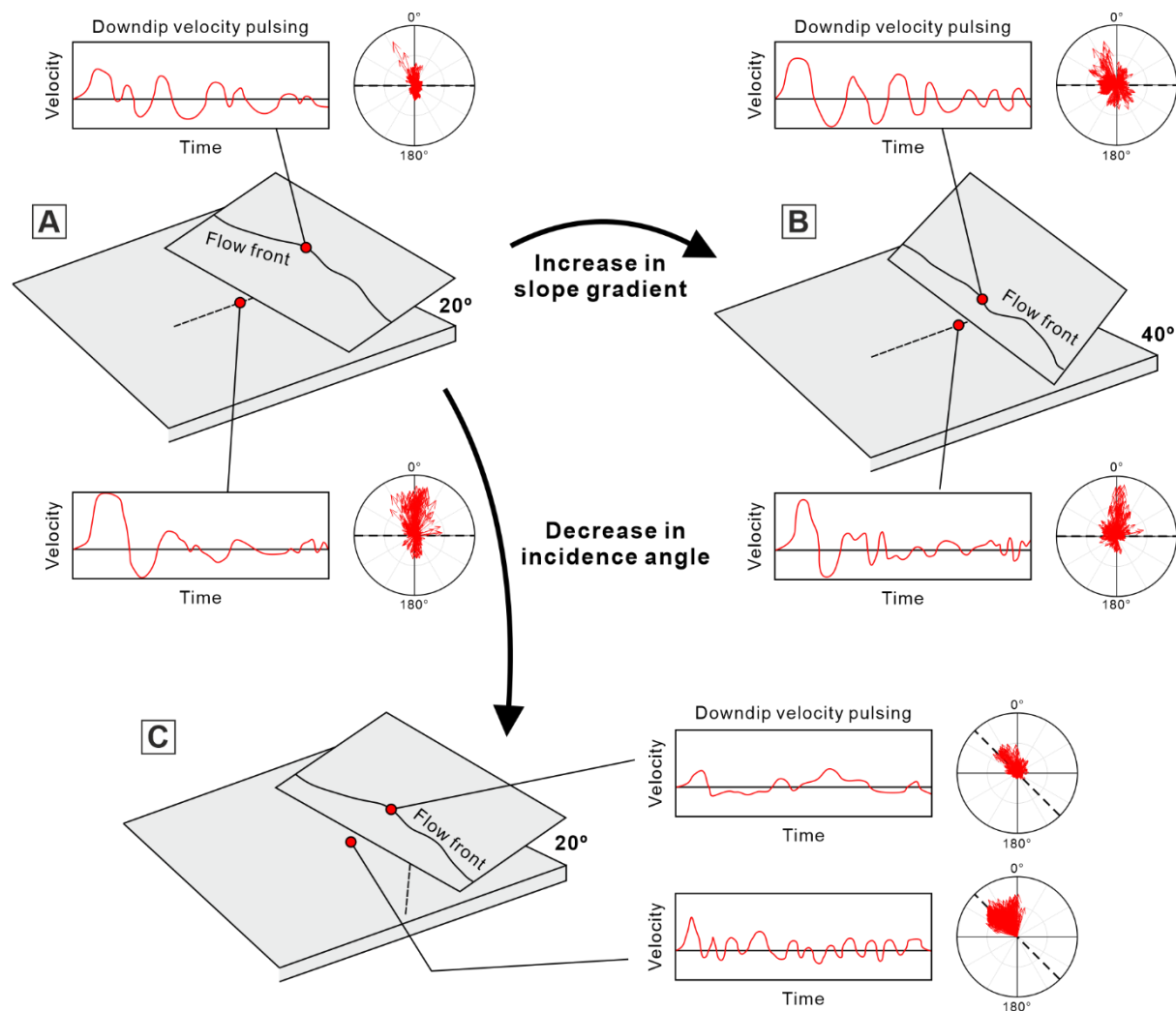


Fig. 17. Schematic diagram illustrating the influence of different containing topographic configurations (orientation and slope gradient) on the temporal pulsing pattern of the down-dip velocity and temporal variability in the velocity vector (based on streamwise and cross-stream velocity). As the incidence angle decreases (A and C), velocity pulsing recorded at the base of slope is characterized by: i) a marked decrease in the magnitude of the maximum velocity U_{max} , ii) a greater number of velocity pulses, and iii) a much shorter duration of each pulse. In cases with a steeper slope gradient (A and B), a subtle decrease in U_{max} , and relatively more and shorter velocity pulses are recorded. Velocity pulsing recorded at the flow front position in experiments with a low flow incidence angle to the slope (A and C) is characterized by a more irregular, non-periodic nature, comparatively fewer and longer velocity pulses. There is

negligible difference in U_{max} , and relatively more and shorter velocity pulses for cases with a steeper slope gradient (A and B).

This mechanism for velocity pulsing on slopes, might potentially be combined with velocity pulsing mechanisms intrinsic to flows such as Kelvin-Helmholtz or Holmboe waves (Kostaschuk et al., 2018), or internal waves (Marshall et al., 2021, 2023). Such pulsing mechanisms are likely at a higher frequency (Kostaschuk et al., 2018), and thus subsidiary to the slope induced pulsing. More complex velocity pulsation may be possible where the flows themselves are driven by externally induced pulsation, such as Rayleigh-Taylor instabilities generated in some plunging flows (Best et al., 2005; Dai, 2008; Kostaschuk et al., 2018), or via other external drivers such as roll waves, storms, and wind- or tide-driven circulation, river discharge events, cyclic slope failure (e.g., Syvitski and Hein, 1991; Ogston and Sternberg, 1999; Ogston et al., 2000; Li et al., 2001; Wright et al., 2002).

Flows that establish velocity pulses will change bed shear stresses and even alternate between periods of sediment erosion and deposition. Therefore, complicated stratigraphic patterns can develop despite quasi-steady inflows (cf. Best et al., 2005). Hence, more and shorter velocity pulses for a single turbidity current event as documented in steeper or less oblique containing slope settings (**Fig. 17**) may lead to complex patterns of sediment deposition, bypass and transient erosion, and hence more intra-bed discontinuities, compared to their counterparts in gentler or highly oblique containing slope settings, respectively. Furthermore, velocity pulsing, and hence fluctuations in flow energy, may be manifested in the rock record with vertical bedform variations when the velocity fluctuations occur across the thresholds of bedform stability fields (Southard, 1991; cf. Ge et al., 2022). Alternations of different bed types representing different flow regimes might occur due to temporal velocity pulsing. For instance, in the rock record, contained turbidites on, or at the base of, slopes can be characterized by

repetitive alternations of internal divisions, including switching between massive or dewatered and laminated, laminated and convoluted, and parallel-laminated and ripple-laminated divisions (e.g., Kneller and McCaffrey, 1999; Felletti, 2002; Muzzi Magalhaes and Tinterri, 2010). Higher frequency velocity pulsing at the base of slopes documented in a steep or lowly oblique containing slope setting (**Fig. 17**) may result in more frequent alternations of internal divisions. The specific type of the internal divisions might be different depending on the magnitude of the near-bed velocity.

Generation and spatial variation of combined flows on slopes

Combined flows in deep-water settings are hypothesised to form as turbidity currents interact with seafloor topography (Kneller et al., 1991; Edwards et al., 1994; Patacci et al., 2015; Tinterri, 2011; Tinterri et al., 2016, 2022; Keavney et al., 2024). The experiments herein (**Fig. 4, Figs 9-11 and Videos 1-4**) support the generation of combined flow in 3D unconfined density current above a topographic slope. This result is consistent with the findings in Keavney et al. (2024) who address the interaction of unconfined density currents with a frontal (i.e., 90-degree incidence angle) containing slope. The combined flow on the slope herein is generated after the unidirectional parental flow transforms upon incidence with the slope into a multidirectional parental flow on the slope surface, which then collapses downslope to converge with the basal dense flow (**Fig. 14 and Videos 1-4**). The combined flow at the flow front positions on the slope is therefore a combination of the newly generated multidirectional outbound flow and the reflected flow downslope. Hence, with this study and Keavney et al. (2024), a new mechanism is demonstrated for generating combined flows across a wide set of topographic slope configurations, without the generation of internal waves as invoked by previous studies (Kneller et al., 1991; Edwards et al., 1994; Patacci et al., 2015; Tinterri, 2011; Tinterri et al., 2016, 2022). Furthermore, in contrast to the regular linear combined flows

generated in confined 2D flume tank experiments (e.g., Pantin and Leeder, 1987; Edwards et al., 1994; Kneller and McCaffrey, 1995; Kneller et al., 1997), the combined flows herein are multidirectional, which should be much more common in nature where flows are free to spread laterally on a topographic slope.

Crucially, this work (**Figs 9-11**) presents a broad range of multidirectional combined flows, the unidirectional component of which varies markedly with different locations on a single containing slope, as well as with different topographic slope configurations (both orientation and slope gradient). Above a single planar slope, as the density current interacts with the topography, the initial unidirectional parental flow is transformed into a strongly multidirectional flow high-up on the slope. Therefore, more radial dispersal patterns in flow direction distribution are noted for the flows documented at the flow front position compared to those recorded at the base of slope (**Fig. 9; Fig. 10A-D** vs. **Fig. 10E-H**). A narrower spread in flow directions along the slope (**Fig. 9A-C**) is likely because the reversing flow at the downstream position tends to collapse downslope and converge with the basal flow running parallel to the slope, likely leading to the establishment of combined flow with a unidirectional component oriented parallel to the slope orientation. In a low flow incidence angle setting, the increased unidirectional component of the flow recorded at the central flow front position high-up on the slope (**Fig. 10A-D**) could be explained by an enhanced influence of flow deflection running parallel to the slope on the flow directions; this is due to a decrease in topographic containment from a near frontal to a highly oblique topographic slope setting (**Fig. 14F**).

This work demonstrates that multiple types of complex multidirectional combined flows can be generated above planar topographic slopes by changing the orientation or slope angle of the containing topographic slope. The interaction of density currents with non-planar seafloor topography and unsteady flows in the field would favour the establishment of even more complex patterns of combined flows above slopes. Therefore, there is no requirement for

reflected bores or internal waves to generate complex combined flows as invoked in field outcrop-based models above complex and/or non-planar topographic slopes (e.g., Tinterri, 2011; Tinterri et al., 2016, 2022).

A new model for deposits on orthogonal and oblique slopes

Formation and spatial distribution of combined flow bedforms on slopes

Combined flow sedimentary structures, including small- to medium-scale biconvex (mega)ripples with internal sigmoidal-cross laminae, and hummock-like bedforms, have been identified in deep-water turbidites at outcrop (e.g., Marjanac, 1990; Haughton, 1994; Remacha et al., 2005; Mulder et al., 2009; Tinterri, 2011; Tinterri et al., 2016, 2022; Hofstra et al., 2018; Martínez-Doñate et al., 2021; Privat et al., 2021; Taylor et al., 2024). The formation of these sedimentary structures is typically hypothesised to be linked to generation of combined flows by the superposition of a unidirectional parental turbidity current with an oscillatory component due to the reflections of the internal waves or bores against a topographic slope (Tinterri, 2011; Tinterri et al., 2016, 2022; see also Kneller et al., 1991; Edwards et al., 1994; Haughton, 1994), largely on the basis of observations of internal waves in 2D or qualitative 3D reflected density current experiments (e.g., Kneller et al., 1991; Edwards et al., 1994). Nevertheless, the present experimental work documents the generation of complex, multidirectional combined flows on the slope surface when unconfined turbidity currents interact with all oblique topographic slope configurations (**Figs 9-11; Videos 1-4**). This is at odds with these previous models, and instead supports the model for the formation of hummock-like bedforms through combined flows on slopes as proposed by Keavney et al. (2024). Herein, this model of Keavney et al. (2024) is demonstrated to be applicable in a wider range of topographic configurations, and a new mechanism for sigmoidal bedforms is proposed, without requirement for an oscillatory component. Hummock-like bedforms form during relatively high sediment fallout rates when

flows decelerate upon incidence with the slope, and under combined flow conditions with a radial dispersal pattern (Keavney et al., 2024). Sigmoidal bedforms form during relatively lower sediment fallout rates, under combined flows with a radial dispersal pattern but a strong unidirectional component.

Depending on the relative strength of the unidirectional component of the multidirectional combined flow documented on slopes in this work (**Figs 9-11** and **Fig. 14**), hummock-like bedforms in these settings are expected to be characterized by various degrees of anisotropy, and transition into symmetric or asymmetric biconvex ripples with internal sigmoidal laminae when the unidirectional component of the combined flow increases. In a single topographic slope, once the particulate density currents encounter the topography, flow decelerates, leading to an increase in suspension fallout rate; the unidirectional parental flow is transformed into a strongly multi-directional flow high-up on the slope. Therefore, more isotropic hummock-like bedforms are predicted to form high-up on the slope under such combined flows (see also Keavney et al., 2024; **Fig. 18A**). Along the in-flow direction high-up on a single slope, the transformed multi-directional flow tends to finally collapse downslope to converge to the basal flow to run parallel to the slope, and hence the combined flow along an in-flow direction tends to show a progressive unidirectional component oriented parallel to the slope (**Fig. 10A-C**). Therefore, more anisotropic hummock-like bedforms, or even sigmoidal bedforms along the slope, are expected to form (**Fig. 18**). Lower on the slope, the superposition of the strong unidirectional parental flow and reflected flow downslope may lead to the deposition of more anisotropic hummock-like bedforms oriented perpendicular to or parallel to the slope depending on the flow incidence angle (**Fig. 18**).

As the flow incidence angle decreases (**Fig. 18A-C**), the enhanced dominance of flow deflection versus reflection (**Fig. 14**) is documented to result in a progressive increase in the unidirectional component of the generated combined flows high-up on the slope (**Fig. 10A-D**).

This in turn may lead to the deposition of hummock-like bedforms characterized by an increased degree of anisotropy (isotropic to strongly anisotropic) or even sigmoidal bedforms when the unidirectional component is very strong. In settings across different slope gradients of the topographic slope, the hummock-like bedforms on the slope surface would not show a marked difference in the degree of anisotropy due to the subtle difference in the types of the generated combined flow (Fig. 11A-C). This means that the degree of anisotropy in hummock-like bedforms is a good indicator of the orientation of the topographic slope, or the flow incidence angle to the topographic slope, but not of the slope gradient.

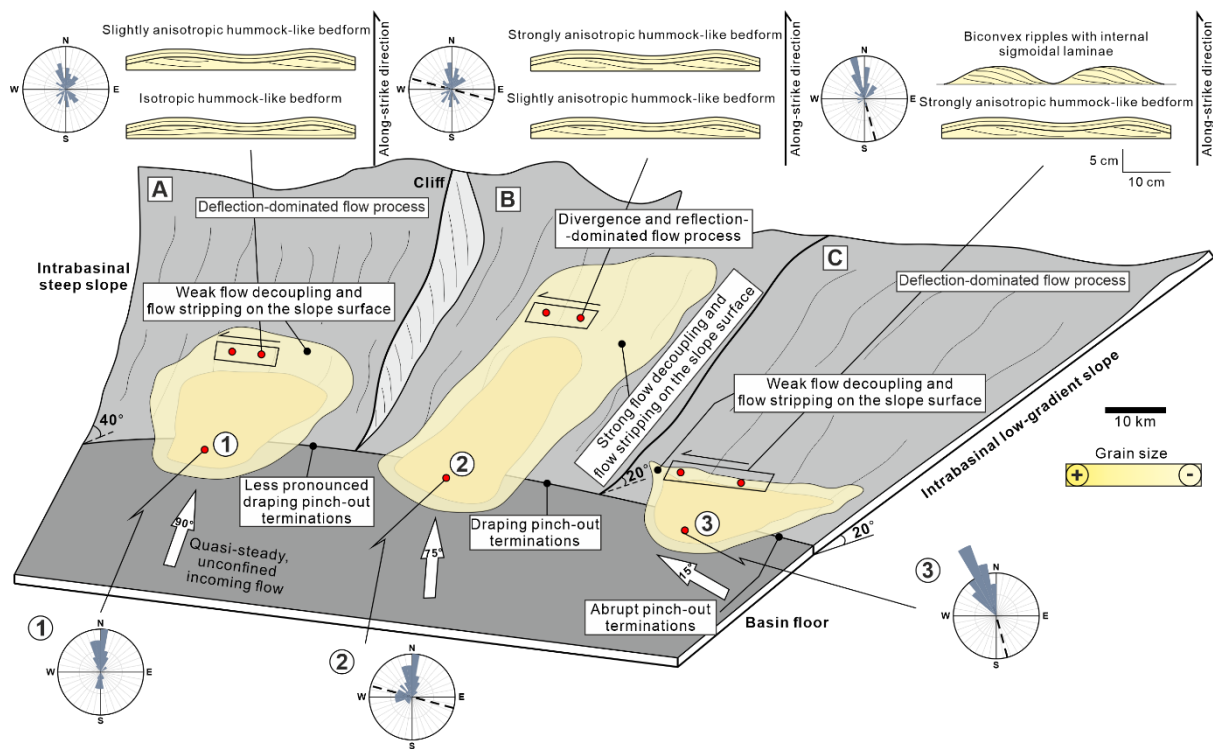


Fig. 18. Schematic diagrams illustrating the model of deposits for the interaction of the 3D unconfined turbidity current with different combinations of containing topographic configurations, including slope gradient and orientation: (A) high-angle intrabasinal slope oriented orthogonal to the incoming flow; (B) low-angle intrabasinal slope oriented nearly orthogonal to the incoming flow; (C) low-angle intrabasinal slope oriented highly oblique to the incoming flow. For each slope configuration, the predicted palaeocurrent distribution

patterns, key types of bedforms, sediment dispersal patterns and onlap styles on slopes are indicated.

General depositional model

The flow process model described herein (**Fig. 14**) is most applicable to basins where the flow volume is smaller than the basin capacity (i.e., unconfined flow) and the flow interacts with high-relief intrabasinal topography with a quasi-steady input flow source. For example, syn- and early post-rift (e.g., Ravnås and Steel, 1997; Cullen et al., 2020) or oblique-slip (Hodgson and Haughton, 2004; Baudouy et al., 2021) settings where fault scarps have a pronounced seabed expression.

For scenarios with a low-gradient intrabasinal slope oriented nearly perpendicular to the incoming flow (**Fig. 18B**), processes are dominated by divergence and reflection (**Fig. 4, 14A and 14D**). The initial flow is observed to decouple into two parts upon incidence of the topographic slope: basal dense region and upper dilute region. The denser basal region of the flow decelerates rapidly at the base of slope due to limited upslope momentum and would therefore lead to the deposition of coarser-grained sediment fraction lower on the slope and abrupt terminations or pinch-outs (Keavney et al., 2024). At the same time, the upper dilute part of the flow can travel higher up on the slope and thin and decelerate on the slope surface, which would result in the deposition of finer-grained sediment fraction draping higher up on the slope surface (Keavney et al., 2024). The combined flows generated above the slope surface would enhance the development of more isotropic hummock-like bedforms.

For scenarios with a low-gradient intrabasinal slope oriented highly oblique to the incoming flow (**Fig. 18C**), the flow process is deflection-dominated with limited upslope momentum and flow-topography interaction (**Video 3 and Fig. 14F**). Weak flow decoupling and flow stripping

on slopes is hypothesized to result in the deposition of a limited zone of draped fines, which abruptly terminates lower on the slope. The combined flows generated above the slope surface would favour the development of more anisotropic hummock-like bedforms or even biconvex ripples with internal sigmoidal laminae oriented parallel to the slope orientation.

For scenarios with an intrabasinal slope of a steeper gradient (**Fig. 18A**), flow is more deflection dominated (**Video 1 and Fig. 14C**). The decreased flow stripping on the slope surface would lead to less pronounced draping of the finer-grained sediment fraction on the slope surface compared to its gentler gradient counterpart (**Fig. 18B**). The rapid flow deceleration at the base of the slope would lead to high rates of suspension fall out and formation of thick coarser-grained sediment fraction, abruptly terminating lower on the slope. In this scenario, an increased relative strength between flow deflection and reflection might lead to a thinner division in sedimentary facies with evidence for flow reflections (**Fig. 18A**) compared to lower-gradient slopes.

The depositional model herein presents the first and most detailed model so far to address the interaction of unconfined turbidity currents and containing topographic slopes. Distinct onlap styles and sedimentary facies in these topographic configurations can be used to reconstruct the orientation and slope gradient of the intrabasinal or basin bounding slopes in the ancient rock record.

CONCLUSIONS

Large-scale 3D physical experiments are utilised to examine the interaction of unconfined density currents with planar slopes at a range of orientations and gradients, and subsequently used to present the implications of the results for sedimentation on submarine slopes. The experiments show that the dominant flow process transitions from divergence-dominated,

through reflection-dominated to deflection-dominated as the flow incidence angle varies from 90° to 15° and the slope gradient changes from 20° to 40°. Patterns of near-bed velocity pulsing at the base of, and on, the slope vary as a function of both the flow incidence angle and slope gradient. In all configurations, complex multidirectional combined flows are observed on, or at the base of, the slope, the types of which are shown to vary spatially across the slope and different configurations of slopes.

The findings challenge the paradigm of flow deflection and reflection in existing flow-topography process models that has stood for three decades. A new process model for flow-slope interactions is presented, which provides new mechanics for the observation of high-angular differences between sole marks and ripple directions documented in many field datasets. A new mechanism for the velocity pulsation on slopes is proposed and the documentation of different patterns of velocity pulsing on slopes across different topographic configurations is presented to attribute to the formation of distinctive stratigraphic patterns in the rock record. The generation and spatial distribution of multiple types of complex multidirectional combined flows on oblique slopes further supports the generation of combined flow in 3D unconfined density current above a topographic slope, in the absence of internal waves or solitons. Specifically, the unidirectional component of the combined flows varies spatially on a slope, as well as with different topographic configurations. This process model provides a novel mechanism for the formation of different types of combined-flow bedforms on a slope and across different slope configurations in deep-sea settings.

The new models of the generation and spatial distribution of combined flows and velocity pulsation patterns, coupled with sediment dispersal patterns and onlap styles on slopes provide an improved model of turbidity current sedimentation on slopes, which can be applied to refine interpretations of exhumed successions. Nonetheless, given the complicated process responses arising from simple topographic configurations documented herein, there remains much to

learn about the interactions of sediment gravity flows and seabed relief, and their depositional expression.

ACKNOWLEDGEMENTS

This research forms a part of the LOBE 3 consortium project, based at University of Leeds and University of Manchester. The authors thank the sponsors of the LOBE 3 consortium project for financial support: Aker BP, BHP, BP, Equinor, HESS, Neptune, Petrobras, PetroChina, Total, Vår Energi and Woodside.

NOMENCLATURE

H_{max} : Maximum run-up height (m)

h : Flow height (m)

Fr : Froude number

Fr_d : Densimetric Froude number

g : Acceleration due to gravity (m s^{-2})

g' : Reduced gravitational acceleration (m s^{-2})

h_p : Height of the maximum downstream velocity above the basin floor (m)

Re : Reynolds number

t : Experimental time since the release of the flow from the mixing tank (s)

U : Mean depth-averaged downstream velocity (m s^{-1})

U_{max} : Maximum velocity over height on the time series profiles of down-dip velocity (m s^{-1})

u : Streamwise velocity or down-dip velocity (m s^{-1})

u_p : Maximum downstream velocity (m s^{-1})

v : Cross-stream velocity or along-strike velocity (m s^{-1})

w : Vertical velocity (m s^{-1})

μ : Dynamic viscosity (Pa s)

ρ_a : Density of the ambient fluid (kg m⁻³)

ρ_s : Mean depth-averaged density of the current (kg m⁻³)

DATA AVAILABILITY STATEMENT

The data that support the findings of this study are available from the corresponding author upon reasonable request. The high-resolution original experimental video files are publicly available and can be downloaded from the GitHub Repository: https://leeds365-my.sharepoint.com/:p/g/personal/earrwa_leeds_ac_uk/EXyljFoj0GZBuIQHux7-dVEBvbqChhhejDVD-F-_QG0Ppw?e=KjyfSJ.

REFERENCES

Alexander, J. and Morris, S. (1994) Observations on experimental, nonchannelized, high-concentration turbidity currents and variations in deposits around obstacles. *J. Sediment. Res.*, **64**, 899-909.

Amy, L.A., McCaffrey, W.D. and Kneller, B.C. (2004) The influence of a lateral basin-slope on the depositional patterns of natural and experimental turbidity currents. In: *Deep-water sedimentation in the Alpine foreland basin of SE France: New perspectives on the Grès d'Annot and related systems* (Eds P. Joseph and S.A. Lomas), *Geol. Soc. London. Spec. Publ.*, **221**, 311-330.

Athmer, W., Groenenberg, R.M., Luthi, S.M., Donselaar, M.E., Sokoutis, D. and Willingshofer, E. (2010) Relay ramps as pathways for turbidity currents: a study combining analogue sandbox experiments and numerical flow simulations. *Sedimentology*, **57**, 806-823.

- 1124 **Azpiroz-Zabala, M., Sumner, E.J., Cartigny, M.J.B., Peakall, J., Clare, M.A., Darby,**
1125 **S.E., Parsons, D.R., Dorrell, R.M., Özsoy, E., Tezcan, D., Wynn, R.B. and Johnson, J.**
1126 (2024) Benthic biology influences sedimentation in submarine channel bends: Coupling of
1127 biology, sedimentation and flow. *The Depositional Record*, **10**, 159-175, doi:
1128 10.1002/dep2.265.
- 1129 **Baas, J.H., Tracey, N.D. and Peakall, J. (2021)** Sole marks reveal deep-marine depositional
1130 process and environment: Implications for flow transformation and hybrid event bed models.
1131 *Journal of Sedimentary Research*, **91**, 986–1009.
- 1132 **Bakke, K., Kane, I.A., Martinsen, O.J., Petersen, S.A., Johansen, T.A., Hustoft, S.,**
1133 **Jacobsen, F.H. and Groth, A. (2013)** Seismic modeling in the analysis of deep-water
1134 sandstone termination styles. *AAPG Bull.*, **97**, 1395-1419.
- 1135 **Baudouy, L., Haughton, P.D. and Walsh, J.J. (2021)** Evolution of a fault-controlled, deep-
1136 water Sub-Basin, Tabernas, SE Spain. *Front. Earth Sci.*, **9**, 767286.
- 1137 **Bell, D., Stevenson, C.J., Kane, I.A., Hodgson, D.M. and Poyatos-Moré, M. (2018)**
1138 Topographic controls on the development of contemporaneous but contrasting basin-floor
1139 depositional architectures. *J. Sed. Res.*, **88**, 1166-1189.
- 1140 **Best, J.L., Kirkbride, A.D. and Peakall, J. (2001)** Mean flow and turbulence structure of
1141 sediment-laden gravity currents: new insights using ultrasonic Doppler velocity profiling. In:
1142 *Particulate Gravity Currents* (Eds W.D. McCaffrey, B.C. Kneller and J. Peakall), *IAS Spec.*
1143 *Publ.*, 31, 159–172.
- 1144 **Best, J.L., Kostaschuk, R.A., Peakall, J., Villard, P.V. and Franklin, M. (2005)** Whole flow
1145 field dynamics and velocity pulsing within natural sediment-laden underflows. *Geology*, **33**,
1146 765-768.

- 1147 **Bruschi, R., Bughi, S., Spinazzè, M., Torselletti, E. and Vitali, L.** (2006) Impact of debris
1148 flows and turbidity currents on seafloor structures. *Norwegian J. Geol.*, **86**, 317–336.
- 1149 **Buckee, C., Kneller, B. and Peakall, J.** (2001) Turbulence structure in steady, solute-driven
1150 gravity currents. In: *Particulate gravity currents* (Eds W. McCaffrey, B. Kneller, J. Peakall),
1151 *Int. Assoc. Sedimentol. Spec. Pub.*, **31**, 173-187.
- 1152 **Carter, L., Gavey, R., Talling, P. and Liu, J.** (2014) Insights into submarine geohazards from
1153 breaks in subsea telecommunication cables. *Oceanography*, **27**, 58–67.
- 1154 **Cartigny, M.J., Ventra, D., Postma, G. and Van Den Berg, J.H.** (2014) Morphodynamics
1155 and sedimentary structures of bedforms under supercritical-flow condition: new insights from
1156 flume experiments. *Sedimentology*, **61**, 712-748.
- 1157 **Chadwick, R., Zweigel, P., Gregersen, U., Kirby, G.A., Holloway, S. and Johannessen, P.**
1158 (2004) Geological reservoir characterization of a CO₂ storage site: The Utsira Sand, Sleipner,
1159 Northern North Sea. *Energy*, **29**, 1371-1381.
- 1160 **Cope, R.N.** (1959) The Silurian rocks of the Devilsbit Mountain district, County Tipperary.
1161 *Proc. Roy. Irish Acad.*, **60**, 217-242.
- 1162 **Craig, G.Y. and Walton, E.K.** (1962) Sedimentary structures and palaeocurrent directions
1163 from the Silurian rocks of Kirkcudbrightshire. *Trans. Edinb. Geol. Soc.*, **19**, 100–119.
- 1164 **Cullen, T.M., Collier, R.E.L., Gawthorpe, R.L., Hodgson, D.M. and Barrett, B.J.** (2020)
1165 Axial and transverse deep-water sediment supply to syn-rift fault terraces: Insights from the
1166 West Xylokastro Fault Block, Gulf of Corinth, Greece. *Basin Res.*, **32**, 1105-1139.
- 1167 **Dai, A.** (2008) Analysis and modeling of plunging flows. PhD thesis, University of Illinois at
1168 Urbana-Champaign, Illinois, US.

- 1169 **Dzulynski, S., Ksiazkiewicz, M. and Kuenen, P. H.** (1959) Turbidites in flysch of the Polish
1170 Carpathian Mountains. *Geol. Soc. Am. Bull.*, **70**, 1089-1118.
- 1171 **Edwards, D.A., Leeder, M.R., Best, J.L. and Pantin, H.M.** (1994) On experimental reflected
1172 density currents and the interpretation of certain turbidites. *Sedimentology*, **41**, 437-461.
- 1173 **Felletti, F.** (2002) Complex bedding geometries and facies associations of the turbiditic fill of
1174 a confined basin in a transpressive setting (Castagnola Fm., Tertiary Piedmont Basin, NW
1175 Italy). *Sedimentology*, **49**, 645-667.
- 1176 **Ge, Z., Nemec, W., Vellinga, A.J. and Gawthorpe, R.L.** (2022) How is a turbidite actually
1177 deposited? *Sci. Adv.*, **8**, eabl9124.
- 1178 **Gilbert, R.** (1975) Sedimentation in Lillooet Lake. *Can. J. Earth Sci.*, **12**, 1697–1711.
- 1179 **Haughton, P.D.** (1994) Deposits of deflected and ponded turbidity currents, Sorbas Basin,
1180 Southeast Spain. *J. Sediment. Res.*, **64**, 233-246.
- 1181 **Haughton, P.D.** (2000) Evolving turbidite systems on a deforming basin floor, Tabernas, SE
1182 Spain. *Sedimentology*, **47**, 497-518.
- 1183 **Haward, M.** (2018) Plastic pollution of the world's seas and oceans as a contemporary
1184 challenge in ocean governance. *Nat. Commun.*, **9**, 667.
- 1185 **Hill, P.R. and Lintern, D.G.** (2022) Turbidity currents on the open slope of the Fraser Delta.
1186 *Marine Geology*, **445**, 106738.
- 1187 **Ho, V.L., Dorrell, R.M., Keevil, G.M., Thomas, R.E., Burns, A.D., Baas, J.H. and**
1188 **McCaffrey, W.D.** (2019) Dynamics and deposition of sediment-bearing multi-pulsed flows
1189 and geological implication. *J. Sediment. Res.*, **89**, 1127-1139.

- 1190 **Hodgson, D.M. and Haughton, P.D.** (2004) Impact of syndepositional faulting on gravity
1191 current behaviour and deep-water stratigraphy: Tabernas-Sorbas Basin, SE Spain. In: *Confined*
1192 *Turbidite Systems* (Eds S.A. Lomas, P. Joseph), *Geol. Soc. Spec. Publ.*, **222**, 135-158.
- 1193 **Hofstra, M., Peakall, J., Hodgson, D.M. and Stevenson, C.J.** (2018) Architecture and
1194 morphodynamics of subcritical sediment waves in ancient channel-lobe transition zone.
1195 *Sedimentology*. **65**, 2339-2367.
- 1196 **Howlett, D.M., Ge, Z., Nemec, W., Gawthorpe, R.L., Rotevatn, A. and Jackson, C.A-L.**
1197 (2019) Response of unconfined turbidity currents to deep-water fold and thrust belt
1198 topography: Orthogonal incidence on solitary and segmented folds. *Sedimentology*, **66**, 2425-
1199 2454.
- 1200 **Kane, I.A., Clare, M.A., Miramontes, E., Wogelius, R., Rothwell, J.J., Garreau, P. and**
1201 **Pohl, F.** (2020) Seafloor microplastic hotspots controlled by deep-sea circulation. *Science*, **368**,
1202 1140-1145.
- 1203 **Keavney, E., Peakall, J., Wang, R., Hodgson, D.M., Kane, I.A., Keevil, G.M., Brown,**
1204 **H.C., Clare, M.A. and Hughes M.** (2024) Flow evolution and velocity structure of unconfined
1205 density currents interacting with frontally containing slopes. *EarthArxiv*, doi:
1206 10.31223/X5CM35.
- 1207 **Keevil, G.M., Peakall, J., Best, J.L. and Amos, K.J.** (2006) Flow structure in sinuous
1208 submarine channels: Velocity and turbulence structure of an experimental submarine channel.
1209 *Mar. Geol.*, **229**, 241-257.
- 1210 **Kelling, G.** (1964) The turbidite concept in Britain. In: *Turbidites (Developments in*
1211 *sedimentology, Volume 3)* (Eds A.H. Bouma and A. Brouwer), pp. 75-92. Elsevier, Amsterdam.

- 1212 **Kneller, B.** (1995) Beyond the turbidite paradigm: physical models for deposition of turbidites
1213 and their implications for reservoir prediction. In: *Characterisation of Deep Marine Clastic*
1214 *Systems* (Eds A.J. Hartley and D.J. Prosser), *Geol. Soc. London. Spec. Publ.*, **94**, 31-49.
- 1215 **Kneller, B. and Buckee, C.** (2000) The structure and fluid mechanics of turbidity currents: a
1216 review of some recent studies and their geological implications. *Sedimentology*, **47**, 62-94.
- 1217 **Kneller, B.C. and McCaffrey, W.D.** (1995) Modelling the effects of salt-induced topography
1218 on deposition from turbidity currents. In: *Salt, sediment and hydrocarbons* (Eds C.J. Travis,
1219 B.C Vendeville, H. Harrison, F.J. Peel, M.R. Hudec, B.E. Perkins), *SEPM Soc. Sediment Geol.*,
1220 137-145.
- 1221 **Kneller, B. and McCaffrey, W.** (1999) Depositional effects of flow nonuniformity and
1222 stratification within turbidity currents approaching a bounding slope: deflection, reflection, and
1223 facies variation. *J. Sed. Res.*, **69**, 980-991.
- 1224 **Kneller, B., Edwards, D., McCaffrey, W. and Moore, R.** (1991) Oblique reflection of
1225 turbidity currents. *Geology*, **14**, 250-252.
- 1226 **Kneller, B.C., Bennett, S.J., and McCaffrey, W.D.** (1997) Velocity and turbulence structure
1227 of density currents and internal solitary waves: potential sediment transport and the formation
1228 of wave ripples in deep water. *Sed. Geol.*, **112**, 235-250.
- 1229 **Konsoer, K., Zinger, J. and Parker, G.** (2013) Bankfull hydraulic geometry of submarine
1230 channels created by turbidity currents: Relations between bankfull channel characteristics and
1231 formative flow discharge. *Journal of Geophysical Research: Earth Surface*, **118**, 216–228,
1232 doi:10.1029/2012JF002422.

- 1233 **Kostaschuk, R., Nasr-Azadani, M.M., Meiburg, E., Wei, T., Chen, Z., Negretti, M.E.,**
1234 **Best, J., Peakall, J. and Parsons, D.R. (2018)** On the causes of pulsing in continuous turbidity
1235 currents. *J. Geophys. Res. Earth Surf.*, **123**, 2827-2843.
- 1236 **Kuenen, P.H. and Migliorini, C.I. (1950)** Turbidity currents as a cause of graded bedding. *J.*
1237 *Geol.*, **58**, 91–127.
- 1238 **Li, G., Tang, Z., Yue, S., Zhuang, K., and Wei, H. (2001)** Sedimentation in the shear front
1239 off the Yellow River mouth. *Cont. Shelf Res.*, 21, 607–625.
- 1240 **Lintern, D.G., Hill, P.R. and Stacey, C. (2016)** Powerful unconfined turbidity current
1241 captured by cabled observatory on the Fraser River delta slope, British Columbia, Canada.
1242 *Sedimentology*, **63**, 1041-1064.
- 1243 **Lloyd, C., Huuse, M., Barrett, B.J. and Newton, A.M.W. (2021)** Regional exploration and
1244 characterisation of CO₂ storage prospects in the Utsira-Skade aquifer, North Viking graben,
1245 North Sea. *Earth Sci. Syst. Soc.*, **1**, 10041.
- 1246 **Lomas, S.A. and Joseph, P. (2004)** Confined turbidite systems. In: *Confined Turbidite Systems*
1247 (Eds S.A. Lomas, P. Joseph), *Geol. Soc. Spec. Publ.*, **222**, 1-7.
- 1248 **Lusseyran, F., Izrar, B., Audemar, C. and Skali-lami, S. (2003)** Time-space characteristics
1249 of stratified shear layer from UVP measurements. *Exp. Fluids*, **35**, 32–40.
- 1250 **Marjanac, T. (1990)** Reflected sediment gravity flows and their deposits in flysch of Middle
1251 Dalmatia, Yugoslavia. *Sedimentology*, **37**, 921-929.
- 1252 **Marshall, C.R., Dorrell, R.M., Keevil, G.M., Peakall, J. and Tobias, S.M. (2021)**
1253 Observations of large-scale coherent structures in gravity currents: implications for flow
1254 dynamics. *Exp. Fluids*, **62**, 120.

- 1255 **Marshall, C.R., Dorrell, R.M., Keevil, G.M., Peakall, J. and Tobias, S.M.** (2023) On the
1256 role of transverse motion in pseudo-steady gravity currents. *Exp. Fluids*, **64**, 63,
1257 doi:10.1007/s00348-023-03599-7.
- 1258 **Martínez-Doñate, A., Privat, A.M-L., Hodgson, D.M., Jackson, C.A-L., Kane, I.A.,**
1259 **Spychala, Y.T., Duller, R.A., Stevenson, C., Keavney, E., Schwarz, E. and Flint, S.S.**
1260 (2021) Substrate entrainment, depositional relief, and sediment capture: impact of a submarine
1261 landslide on flow process and sediment supply. *Front. Earth. Sci.*, **9**, 757617.
- 1262 **McCaffrey, W.D. and Kneller, B.C.** (2001) Process controls on the development of
1263 stratigraphic trap potential on the margins of confined turbidite systems and aids to reservoir
1264 evaluation. *AAPG Bull.*, **85**, 971-988.
- 1265 **Middleton, G.V.** (1993) Sediment deposition from turbidity currents. *Annu. Rev. Earth Planet.*
1266 *Sci.*, **21**, 89–114.
- 1267 **Muck, M.T. and Underwood, M.B.** (1990) Upslope flow of turbidity currents: a comparison
1268 among field observations, theory, and laboratory methods. *Geology*, **18**, 54–57.
- 1269 **Mulder, T., Razin, P. and Faugeres, J-C.** (2009) Hummocky cross-stratification-like
1270 structures in deep-sea turbidites: Upper Cretaceous Basque basins (Western Pyrenees, France).
1271 *Sedimentology*, **56**, 997–1015.
- 1272 **Muzzi Magalhaes, P. and Tinterri, R.** (2010) Stratigraphy and depositional setting of slurry
1273 and contained (reflected) beds in the Marnoso-Arenacea Formation (Langhian-Serravallian)
1274 Northern Apennines, Italy. *Sedimentology*, **57**, 1685–1720.
- 1275 **Normark, W.R., Posamentier, H. and Mutti, E.** (1993) Turbidite systems: state of the art and
1276 future directions. *Rev. Geophys.*, **31**, 91-116.

- 1277 **Ogston, A.S. and Sternberg, R.W.** (1999) Sediment-transport events on the northern
1278 California continental shelf. *Mar. Geol.*, **154**, 69–82.
- 1279 **Ogston, A.S., Cacchione, D.A., Sternberg, A.S. and Kineke, G.C.** (2000) Observations of
1280 storm and river flood-driven sediment transport on the northern California continental shelf.
1281 *Cont. Shelf Res.*, 20, 2141–2162.
- 1282 **Pantin, H.M. and Leeder, M.R.** (1987) Reverse flow in turbidity currents: the role of internal
1283 solitons. *Sedimentology*, **34**, 1143-1155.
- 1284 **Patacci, M., Haughton, P.D.W. and McCaffrey, W.D.** (2015) Flow behaviour of ponded
1285 turbidity currents. *J. Sed. Res.*, **85**, 885-902.
- 1286 **Peakall, J., Ashworth, P. and Best, J.** (1996) Physical modelling in fluvial geomorphology:
1287 principles, applications and unresolved issues, in *The Scientific Nature of Geomorphology:*
1288 *proceedings of the 27th Binghamton symposium, September 27-29, 1996.* (Eds B. Rhoads and
1289 C. Thorn) (Hoboken, NJ: Wiley and Sons Ltd), 221-253.
- 1290 **Peakall, J., Best, J.L., Baas, J., Hodgson, D.M., Clare, M.A., Talling, P.J., Dorrell, R.M.**
1291 **and Lee, D.R.** (2020) An integrated process-based model of flutes and tool marks in deep-
1292 water environments: implications for palaeohydraulics, the Bouma sequence, and hybrid event
1293 beds. *Sedimentology*, **67**, 1601–1666, 10.1111/SED.12727.
- 1294 **Pickering, K.T. and Hiscott, R.H.** (1985) Contained (reflected) turbidity currents from the
1295 Middle Ordovician Cloridorme Formation, Quebec, Canada: an alternative to the antidune
1296 hypothesis. *Sedimentology*, **32**, 373-394.
- 1297 **Prentice, J.E.** (1962) The sedimentary history of the Carboniferous in Devon. In: *Some aspects*
1298 *of the Variscan fold belt* (Ed. K. Coe), pp. 93-108. Manchester University Press, Manchester,
1299 England.

- 1300 **Privat, A.M-L.J., Hodgson, D.M., Jackson, C.A-L., Schwarz, E. and Peakall, J. (2021)**
 1301 Evolution from syn-rift carbonates to early post-rift deep-marine intraslope lobes: The role of
 1302 rift basin physiography on sedimentation patterns. *Sedimentology*, **68**, 2563-2605.
- 1303 **Ravnås, R. and Steel, R.J. (1997)** Contrasting styles of Late Jurassic syn-rift turbidite
 1304 sedimentation: a comparative study of the Magnus and Oseberg areas, northern North Sea.
 1305 *Mar. Petrol. Geol.*, **14**, 417-449.
- 1306 **Remacha, E., Fernandez, L.P. and Maestro, E. (2005)** The transition between sheet-like lobe
 1307 and basin-plain turbidites in the Hecho Basin (South-Central Pyrenees, Spain). *J. Sed. Res.*, **75**,
 1308 798-819.
- 1309 **Scott, K.M. (1967)** Intra-bed palaeocurrent variations in a Silurian flysch sequence,
 1310 Kircudbrightshire, Southern Uplands of Scotland. *Scott. J. Geol.*, **3**, 268-281.
- 1311 **Seilacher, A. and Meischner, D. (1965)** Fazies-analyse im palaozoikum des Oslo-Gebeites.
 1312 *Geologische Rundschau*, **54**, 596-619.
- 1313 **Sequeiros, O.E., Spinewine, B., Beaubouef, R.T., Sun, T., Garcia, M.H. and Parker, G.**
 1314 (2010) Bedload transport and bed resistance associated with density and turbidity
 1315 currents. *Sedimentology*, **57**, 1463-1490.
- 1316 **Sestini G. (1970)** Flysch facies and turbidite sedimentology. *Sediment. Geol.*, **4**, 559–597.
- 1317 **Simmons, S.M., Azpiroz-Zabala, M., Cartigny, M.J.B., Clare, M.A., Cooper, C., Parsons,**
 1318 **D.R., Pope, E.L., Sumner, E.J. and Talling, P.J. (2020).** Novel acoustic method provides first
 1319 detailed measurements of sediment concentration structure within submarine turbidity currents.
 1320 *Journal of Geophysical Research: Oceans*, **125**, e2019JC015904, doi: 10.1029/2019JC015904.
- 1321 **Sinclair, H.D. (1994)** The influence of lateral basinal slopes on turbidite sedimentation in the
 1322 Annot Sandstones of SE France. *J. Sediment. Res.*, **64**, 42–54.

- 1323 **Smith, R.D.A. and Anketell, J.M.** (1992) Welsh Basin ‘contourites’ reinterpreted as fine-
1324 grained turbidites: the Grogal Sandstones. *Geological Magazine*, **129**, 609-614.
- 1325 **Southard, J.B.** (1991) Experimental determination of bed-form stability. *Annu. Rev. Earth*
1326 *Planet. Sci.*, **19**, 423-455.
- 1327 **Southern, S.J., Patacci, M., Felletti, F. and McCaffrey, W.D.** (2015) Influence of flow
1328 containment and substrate entrainment upon sandy hybrid event beds containing a co-genetic
1329 mud-clast-rich division. *Sediment. Geol.*, **321**, 105-122.
- 1330 **Soutter, E.L., Bell, D., Cumberpatch, Z.A., Ferguson, R.A., Spychala, Y.T., Kane, I.A.**
1331 **and Eggenhuisen, J.T.** (2021) The influence of confining topography orientation on
1332 experimental turbidity currents and geological implications. *Front. Earth. Sci.*, **8**. 540633.
- 1333 **Stevenson, C.J., Talling, P.J., Wynn, R.B., Masson, D.G., Hunt, J.E., Frenz, M.,**
1334 **Akhmetzhanov, A. and Cronin, B.T.** (2013) The flows that left no trace: Very large-volume
1335 turbidity currents that bypassed sediment through submarine channels without eroding the sea
1336 floor. *Marine and Petroleum Geology*, **41**, 186-205.
- 1337 **Sumner, E.J., Peakall, J., Dorrell, R.M., Parsons, D.R., Darby, S.E., Wynn, R.B.,**
1338 **McPhail, S.D., Perrett, J., Webb, A., and White D.** (2014) Driven around the bend: spatial
1339 evolution and controls on the orientation of helical bend flow in a natural submarine gravity
1340 current. *Journal of Geophysical Research – Oceans*, **119**, 898-913, doi:
1341 10.1002/2013JC009008.
- 1342 **Syvitski, J.P.M. and Hein, F.J.** (1991) Sedimentology of an Arctic basin: Itirbilung Fiord,
1343 Baffin Island, Northwest Territories. *Geological Survey of Canada Paper*, **90**, 66.
- 1344 **Takeda, Y.** (1991) Development of an Ultrasound Velocity Profile Monitor. *Nucl. Eng. Des.*,
1345 **126**, 277–284.

- 1346 **Takeda, Y.** (1993) Velocity Profile Measurement by Ultrasonic Doppler Method. In:
1347 *Experimental Heat Transfer, Fluid Mechanics and Thermodynamics* (Ed. M.D. Kelleher), pp.
1348 126–131. Elsevier, Amsterdam.
- 1349 **Taylor, W.J., Hodgson, D.M., Peakall, J., Kane, I.A., Morris, E.A. and Flint, S.S.** (2024)
1350 Unidirectional and combined transitional flow bedforms: Controls on process and distribution
1351 in submarine slope settings. *Sedimentology*, doi: 10.1111/sed.13177.
- 1352 **Thomas, R.E., Schindfessel, L., McLelland, S.J., Creëlle, S. and De Mulder, T.** (2017) Bias
1353 in mean velocities and noise in variances and covariances measured using a multistatic acoustic
1354 profiler: The Nortek Vectrino Profiler. *Meas. Sci. Technol.*, **28**, 075302, 25p.
- 1355 **Tinterri, R.** (2011) Combined flow sedimentary structures and the genetic link between
1356 sigmoidal- and hummocky-cross stratification. *GeoActa*, **10**, 43-85.
- 1357 **Tinterri, R. and Muzzi Magalhaes, P.** (2011) Synsedimentary structural control on foredeep
1358 turbidites related to basin segmentation: facies response to the increase in tectonic confinement
1359 (Marnoso-arenacea Formation, Miocene, Northern Apennines, Italy). *Mar. Petrol. Geol.*, **67**,
1360 81-110.
- 1361 **Tinterri, R., Muzzi Magalhaes, P., Tagliaferri, A. and Cunha, R.S.** (2016) Convolute
1362 laminations and load structures in turbidites as indicators of flow reflections and decelerations
1363 against bounding slopes. Examples from the Marnoso-arenacea Formation (northern Italy) and
1364 Annot Sandstones (south eastern France). *Sed. Geol.*, **344**, 382-407.
- 1365 **Tinterri, R., Mazza, T. and Muzzi Magalhaes, P.** (2022) Contained-reflected megaturbidites
1366 of the Marnoso-arenacea Formation (Contessa Key Bed) and Helminthoid Flysches (Northern
1367 Apennines, Italy) and Hecho Group (South-Western Pyrenees). *Front. Earth. Sci.*, **25**, 817012.

Tóké, L. and Patacci, M. (2018) Quantifying tabularity of turbidite beds and its relationship to the inferred degrees of basin confinement. *Mar. Petrol. Geol.*, **97**, 659-671.

Wei, T., Peakall, J., Parsons, D.R., Chen, Z., Zhao, B. and Best, J.L. (2013) Three-dimensional gravity-current flow within a subaqueous bend: Spatial evolution and force balance variations. *Sedimentology*, **60**, 1668–1680.

Wright, L.D., Friedrichs, C.T., and Scully, M.E. (2002) Pulsational gravity-driven sediment transport on two energetic shelves. *Cont. Shelf Res.*, **22**, 2443–2460.

Yalin, M. S. (1971) Theory of hydraulic models. Macmillan, London, United Kingdom, 266pp.

SUPPLEMENTARY TEXT

Supporting Information 1: Derivation of the input parameters for the estimation of the Flow Reynolds number and densimetric Froude number

Flow Reynolds number and densimetric Froude number were estimated for the experimental density current recorded at 3 m downstream from the channel mouth along the channel-basin centreline in the unconfined reference experiment. They were computed by Equations 1, 3 and 4 (see main text), with input parameters shown in **Table 2**.

Notably, the overall flow height h (0.11 m) was observed directly from the time-averaged profiles of downstream velocity (**Fig. 3G**) at the measurement position, where the downstream velocity recorded by the UVP reaches zero at the top of the flow. Additionally, two input parameters were calculated from the time-averaged profiles of downstream velocity and density (**Fig. 3G**) at this position: depth-averaged downstream velocity U , and depth-averaged density of the current ρ_s . They were estimated by averaging the velocity or density values recorded or extrapolated at regularly spaced height intervals (0.05 m) over the full depth of the flow, respectively.

SUPPLEMENTARY FIGURES AND TABLES

TABLE S1. Set-up parameters for the Ultrasonic Velocity Profiler (UVP) and Acoustic Doppler Velocimeter (ADV).

UVP parameters		ADV parameters	
Instrument	Met-Flow UVP Monitor 4	Instrument	Vectrino Doppler Velocimeter
Frequency	4 Hz	Frequency	100 Hz
Ultrasound speed in water	1480 m s ⁻¹	Sound speed in water	1480 m s ⁻¹
Number of channels	128	Number of transducers	4
Number of profiles	1000	Range to first cell	0.040 m
Sampling period	11 ms	Range to last cell	0.070 m
Axis velocity range	0.256 m s ⁻¹	Cell size	0.001 m

Minimum axis velocity	-0.128 m s ⁻¹	Number of cells	31
Maximum axis velocity	0.128 m s ⁻¹	Streamwise velocity range	0.300 m s ⁻¹
Minimum measurement distance	4.995 mm	Horizontal velocity range	1.399 m s ⁻¹
Maximum measurement distance	99.715 mm	Vertical velocity range	0.372 m s ⁻¹